DOE/ET-53088-180 IFSR #**180**

Role of Impurity Dynamics in Resistivity-Gradient-Driven Turbulence and Tokamak Edge Plasma Phenomena

T. S. Hahm, P. H. Diamond, P. W. Terry
Institute for Fusion Studies
The University of Texas at Austin
Austin, Texas 78712-1060

and

L. Garcia and *B. A. Carreras*
Oak Ridge National Laboratory
Oak Ridge, TN 37831

March 1986

Role of Impurity Dynamics in Resistivity-Gradient-Driven Turbulence and Tokamak Edge Plasma Phenomena

T.S. Hahm, P.H. Diamond, P.W. Terry

Institute for Fusion Studies

The University of Texas at Austin

Austin, Texas 78712

and

L. Garcia and B.A. Carreras

Oak Ridge National Laboratory

Oak Ridge, Tennessee 37831

Abstract

The role of impurity dynamics in resistivity gradient driven turbulence is investigated in the context of modeling tokamak edge plasma phenomena. The effects of impurity concentration fluctuations and gradients on the linear behavior of rippling instabilities and on the nonlinear evolution and saturation of resistivity gradient driven turbulence are studied both analytically and computationally. At saturation, fluctuation levels and paraticle and thermal diffusivities are calculated. In particular, the mean-square turbulent radial velocity is given by $\langle \hat{v}_r^2 \rangle = (E_0 L_s / B_z)^2 \left(L_\eta^{-1} + L_z^{-1} \right)^2$. Thus, edged peaked impurity concentrations tend to enhance the turbulence, while axially peaked concentrations tend to quench it. The theoretical predictions are in semi-quantitative agreement with experimental results from the TEXT [Bull. Am. Phys. Soc. **30**, 1443 (1985)], Caltech [Phys. Fluids **29**, 309 (1986)], and Tosca [the $12th$ European Conference on Controlled Fusion and Plasma Physics Vol. I, p. 311 (European Physical Society, Budapest, 1985)] tokamaks. Finally, a theory of the density clamp observed during CO-NBI on the ISX-B tokamak [Plasma Physics and Controlled Nuclear Fusion Research, Vol. I, p. 377 (JAEA, Vienna, 1981)] is proposed.

I. Introduction

It is well known that tokamak edge plasmas are strongly turbulent, with large density and electrostatic potential fluctuations[1-5] and large particle diffusivity[6-8] frequently being observed. Understanding tokamak edge turbulence is important in order to optimize limiter and divertor design, and in order to exploit improved confinement regimes, such as the ASDEX H-mode,[9] which are sensitive to conditions at the plasma boundary. However, in view of the accessibility of edge plasmas to electrostatic and magnetic probes, tokamak edge turbulence is also an excellent trial model or test case for theories of plasma turbulence and anomalous transport.

One theory of edge fluctuation dynamics is based on resistivity gradient driven (rippling mode) turbulence.[10] This model is described by reduced, resistive magnetohydrodynamics and a resistivity evolution

$$\tilde{E}_{\|} = \eta_0 \tilde{J}_z + \tilde{\eta} J_{z0}$$

$$\rho_m d\nabla_{\perp}^2 \phi/dt = B_z \nabla_{\|} \tilde{J}_z$$

$$d\tilde{\eta}/dt - \chi_T \nabla_{\|}^2 \tilde{\eta} = -\hat{v}_r d\eta_0/dr,$$

where $\hat{v}_r$ is the radial $\mathbf{E} \times \mathbf{B}$ convection. Fluctuations are driven by the resistivity gradient via Ohm's law and the Lorentz force term of the vorticity evolution equation. While this model has been shown to have many attractive qualitative features,[10] the stabilizing effect of parallel thermal conduction χ_T severely limits the range of applicability of the theory. However, recent theoretical and computational investigations[11] have demonstrated that the predicted fluctuation levels and diffusivity are, in fact, relatively insensitive to χ_T. This rather counterintuitive result is a consequence of the departure of nonlinearly evolving resistivity gradient driven turbulence from its linear antecedent, the rippling instability.[12] In particular, the radially asymmetric mode structure is nonlinearly modified, so that the resistivity $\tilde{\eta}$ and potential ϕ perturbations decouple from the current perturbation $\tilde{J}_z$. Hence, $\tilde{J}_z \sim 0$ in the region of interest, so that the nonlinear evolution of resistivity gradient driven turbulence is described by the equations

$$-B_z \nabla_{\|} \phi \cong \tilde{\eta} J_{z0}$$

$$\frac{d\tilde{\eta}}{dt} - \chi_T \nabla_{\|}^2 \tilde{\eta} = -\hat{v}_r \frac{d\eta_0}{dr}$$

Note that one consequence of current decoupling is that the vorticity equation is eliminated from the nonlinear dynamics. As a result, the characteristic radial scale $\Delta_{\mathbf{k}}$ is determined by thermal conduction and cross-field, turbulent diffusion, so that $\Delta_{\mathbf{k}} = \left(D_{\mathbf{k}}/\chi_T k_{\|}'^2\right)^{1/4}$, where $D_{\mathbf{k}}$ is the cross-field diffusivity of the resistive perturbation and $k_{\|}' = k_y/L_s$, L_s is the shear length. Saturation occurs when $D_{\mathbf{k}}$ and $\Delta_{\mathbf{k}}$ adjust so that resistivity gradient drive $\langle \hat{v}_r \tilde{\eta} \rangle_{\mathbf{k}} \, d\eta_0/dr$ balances thermal dissipation $\chi_T \langle (\nabla_{\|} \tilde{\eta})^2 \rangle_{\mathbf{k}}$. Thus, at saturation, $D_{\mathbf{k}} \cong (L_s E_0/L_\eta B_z)^{4/3} \left(\chi_T k_{\|}'^2\right)^{-1/3}$. The weak dependence of $D_{\mathbf{k}}$ on χ_T is indicative of the qualitative difference between the linear and nonlinear dynamics of the resistivity-gradient-driven turbulence model.

Prior investigations[10-13] of rippling modes have dealt primarily with thermal resistivity fluctuations, driven by temperature gradients. In this paper, a model of resistivity gradient turbulence which incorporates both impurity density (Z_{eff}) and temperature fluctuations and gradients is discussed. As originally proposed by Rutherford,[14] fluctuations in the density of low-Z impurities in a dirty plasma ($Z_{\text{eff}} \gtrsim 2$) result in Z_{eff} fluctuations which in turn drive rippling instabilities. Thus, for $\eta = Z_{\text{eff}} \eta_{\text{sp}}$, where η_{sp} is the Spitzer resistivity,

$$\tilde{\eta} = Z_{\text{eff}} \left(\frac{d\eta_{\text{sp}}}{dT} \right) \tilde{T} + \tilde{Z}_{\text{eff}} \eta_{\text{sp}}.$$

For the prototypical case of a single, low-Z impurity species, the Z_{eff} fluctuation dynamics are described by

$$\frac{d}{dt} \tilde{Z}_{\text{eff}} - \chi_z \nabla_{\|}^2 \tilde{Z}_{\text{eff}} = -\hat{v}_r \frac{dZ_{\text{eff}}(r)}{dr}.$$

The parallel diffusion operator $\chi_z \nabla_{\|}^2$ is a consequence of the fact that parallel impurity flow is determined by the balance of the parallel impurity pressure gradient with impurity-ion friction. Thus, the $\tilde{Z}_{\text{eff}}$ evolution equation can be included along with Ohm's law, the vorticity equation and the temperature evolution equation in a more complete model of resistivity gradient driven turbulence. Indeed, since $\chi_z = v_{Ti}^2/Z^2 \nu_{ii} \ll \chi_T$, impurity-gradient-driven rippling modes are significantly more robust than their temperature-gradient-driven analogues.

In this paper, the role of impurity dynamics in resistivity gradient driven turbulence and tokamak edge plasma phenomena is discussed. A key difference between impurity

and temperature dynamics is that in contrast to $\eta_{\rm sp}(r)$, which virtually always increases with radius, the $Z_{\rm eff}(r)$ profile may peak either on axis or at the edge. Thus, the impurity gradient can either enhance (edge-peaked $Z_{\rm eff}(r)$) or oppose (axially-peaked $Z_{\rm eff}(r)$) the temperature gradient drive. However, since $\chi_z \ll \chi_T$, the impurity dynamics determine the linear evolution of the rippling instability. Nonlinearly, the decoupling of $\tilde{J}_z$ from $\tilde{\eta}_{\rm sp}, \phi$ and $\tilde{Z}_{\rm eff}$ results in a simplified set of renormalized equations

$$
\begin{aligned}
-B_z \nabla_{\|} \phi &= \tilde{Z}_{\rm eff} \eta_{\rm sp} J_0 + Z_{\rm eff} \tilde{\eta}_{\rm sp} J_0 \\
-\chi_T \nabla_{\|}^2 \tilde{\eta}_{\rm sp} - D^T \frac{\partial^2 \tilde{\eta}_{\rm sp}}{\partial x^2} &= -\hat{v}_r \frac{d\eta_0}{dt} \\
-\chi_z \nabla_{\|}^2 \tilde{Z}_{\rm eff} - D^z \frac{\partial^2 \tilde{Z}_{\rm eff}}{\partial x^2} &= -\hat{v}_r \frac{dZ_{\rm eff_0}}{dr}
\end{aligned}
$$

which describe saturated resistivity-gradient-driven turbulence. The mean-square turbulent radial velocity derived via nonlinear calculation is given by $\left\langle \hat{v}_r^2 \right\rangle = \left(L_s E_0 (1+\eta_z)/L_\eta B_z\right)^2$. Thus, while $\eta_z > 0 (\eta_z < 0)$ indeed tends to enhance (quench) the turbulence, the insensitivity of the saturated state to parallel transport is manifested by the relatively modest value of the ratio $D^z/D^T \sim (\chi_T/\chi_z)^{1/3} \sim (m_i/m_e)^{1/6}$. Therefore, the principal consequences of the inclusion of impurity dynamics in the resistivity-gradient-driven turbulence model are an increase in the domain of linear instability and the possibility of meaningful estimates of density mixing lengths and fluctuation levels.

The principal results of this investigation can be summarized as follows:

i) The basic resistivity gradient turbulence model[11] has been extended to include impurity dynamics. Impurity concentration profiles peaked at the edge (on axis) tend to enhance (quench) the turbulence. In most cases, the impurity dynamics dominate the linear evolution of resistivity gradient driven turbulence.

ii) The saturated fluctuation levels and thermal and impurity diffusivities have been calculated and the density, temperature, and potential fluctuation levels have been determined. . The predictions of the analytic theory are in good agreement with the results of nonlinear, multiple helicity calculations. In particular, $\tilde{n}/n_0 \gg \tilde{T}/T_0$, $\tilde{n}/n_0 \neq e\Phi/T_0$, and typically $\dfrac{\tilde{n}}{n_0} \gtrsim .2$ while increasing as $r \to a$. These properties are consistent with results from studies of tokamak edge turbulence.[4]

iii) The cross-field particle diffusivity has been calculated, and is given by

$$D_n \cong \left[\frac{E_0}{B_z}\frac{L_s}{L_\eta}(1+\eta_z)\right]^{4/3}\left(\chi_z \bar{k}_\parallel'^{\,2}\right)^{-1/3}$$
$$\sim T^{-5/6} n^{1/3} B_z^{-4/3}\,\frac{q^2R^2}{\hat{s}^2} V_L^{4/3}\,(1/L_\eta + 1/L_z)^{4/3}\,,$$

where q and $\hat{s}$ have the usual meaning of safety factor and shear. Note that typically $D_n \gtrapprox 10^4 \mathrm{cm}^2/\mathrm{sec}$ and that $D_n(r)$ increases as $r \to a$. Also, D_n scales favorably with plasma current and unfavorably (for q not held fixed) with B_z. Calculation of magnetic fluctuation levels and the associated thermal diffusivity indicates that the dominant thermal transport mechanism is convection; i.e., $Q = T\Gamma_n$. These predictions are consistent with results from experiments on the TEXT[6] and Caltech[7] and Tosca[8] tokamaks, respectively.

iv) A mechanism which explains the density clamp[15] observed during neutral beam co-injection in terms of an impurity gradient-induced enhancement of the particle diffusivity is proposed. This mechanism requires that $Z_{\mathrm{eff}}(r)$ be peaked at the edge.

The remainder of this paper is organized as follows. The basic theoretical model of resistivity-gradient-driven turbulence with impurity dynamics is discussed in Sec. II. In Sec. III, the linear theory is presented. The nonlinear evolution and saturation of resistivity-gradient-driven turbulence are discussed in Sec. IV. Fluctuation levels and anomalous transport coefficients are discussed in Sec. V. Section VI contains a discussion of applications of the theory to tokamak edge plasma phenomena. In Sec. VII, a summary and conclusions are set forth.

II. Theoretical Model

The reduced resistive magnetohydrodynamic (MHD) equations in cylindrical geometry[16] are

$$E_{\parallel} = \frac{\partial \psi}{\partial t} - B_z \nabla_{\parallel} \phi = \eta J_z, \tag{1}$$

$$\frac{dU}{dt} = B_z \nabla_{\parallel} J_z, \tag{2}$$

where ψ is the poloidal flux function, ϕ is the fluid stream function ($\phi = \Phi/B_z$, where Φ is the electrostatic potential), J_z is the current density,

$$J_z = \frac{1}{\mu_0} \nabla_{\perp}^2 \psi,$$

and U is the component of the vorticity in the z-direction

$$U = \vec{\nabla}_{\perp} \cdot (\rho_m \vec{\nabla}_{\perp} \phi).$$

The coordinate z is taken to extend along the axis of the cylinder; ρ_m is the mass density. In Eqs. (1) and (2),

$$\frac{d}{dt} \equiv \frac{\partial}{\partial t} + (\vec{\nabla}_{\perp} \phi \times \hat{z}) \cdot \vec{\nabla}$$

and

$$B_z \nabla_{\parallel} \equiv (\vec{\nabla}_{\perp} \psi \times \hat{z}) \cdot \vec{\nabla} + B_z \frac{\partial}{\partial z}$$

are the total convective derivative and the parallel gradient. To describe rippling instabilities, a resistivity evolution (thermal balance) equation is necessary. Moreover, in a plasma with a significant level of impurities, the resistivity η will depend not only on T_e but also on the quantity $Z_{\text{eff}} = 1 + Z^2 n_I / n_o$. For simplicity, we assume that only one impurity species is present having charge Z, and density n_I i.e., $\eta = \eta_{\text{sp}}(T_e) Z_{\text{eff}}$. Hence, two equations; one for $\eta_{\text{sp}}(T_e)$ and the other for Z_{eff}, describe the resistivity evolution. The equations are:

$$\frac{d}{dt} \eta_{\text{sp}} = \nabla_{\parallel} \chi_T \nabla_{\parallel} \eta_{\text{sp}}, \tag{3}$$

$$\frac{d}{dt} Z_{\text{eff}} = \nabla_{\parallel} \chi_z \nabla_{\parallel} Z_{\text{eff}}, \tag{4}$$

where $\eta_{\text{sp}} = m_e \nu_{ei}(T_e)/n_0 e^2$ is the Spitzer resistivity, χ_T is the parallel electron thermal conductivity, and $\chi_z = v_{th,i}^2 / Z^2 \nu_{ii}$ is the effective transport coefficient for impurity ion

flow along field lines, resulting from the balance of the parallel impurity pressure gradient with impurity-ion friction.

Equation (4) has been derived from an impurity dynamics model proposed by Rutherford[14] and only a summary of the derivation is given in the appendix. Equations (1)-(4) together with the relation $\eta = \eta_{\rm sp} Z_{\rm eff}$, constitute the basic impurity-gradient-driven turbulence model. These equations are used without further approximation for the numerical calculations described in this paper. To facilitate analytic calculations we further simplify this basic model by introducing the electrostatic approximation, i.e., $\tilde{\psi} = 0$ and $\nabla_\parallel = \nabla_\parallel^{(0)} = \hat{b} \cdot \vec{\nabla}$, where the vector $\hat{b}$ is a unit vector parallel to the equilibrium magnetic field. The validity of this approximation for rippling instabilities was discussed in Ref. (11). Employing the electrostatic approximation and writing J_z, $\eta_{\rm sp}$, and $Z_{\rm eff}$ as a sum of average (indicated by subscript 0) and perturbed (indicated by tilde $\sim$) pieces, Eqs. (1)-(4) become, for $\tilde{\eta} = \tilde{\eta}_{\rm sp} Z_{\rm eff,0} + \eta_{\rm sp,0} \tilde{Z}_{\rm eff}$

$$-B_z \nabla_\parallel^{(0)} \phi = \tilde{\eta} J_{z0} + \eta_0 \tilde{J}_z, \tag{5}$$

$$\rho_m \frac{d}{dt} \nabla_\perp^2 \phi = B_z \nabla_\parallel^{(0)} \tilde{J}_z, \tag{6}$$

$$\frac{d\tilde{\eta}_{\rm sp}}{dt} - \chi_T \nabla_\parallel^{(0)^2} \tilde{\eta}_{\rm sp} = -\frac{1}{r} \frac{\partial \phi}{\partial \theta} \frac{d\eta_{\rm sp,0}}{dr}, \tag{7}$$

$$\frac{d}{dt} \tilde{Z}_{\rm eff} - \chi_Z \nabla_\parallel^{(0)^2} \tilde{Z}_{\rm eff} = -\frac{1}{r} \frac{\partial \phi}{\partial \theta} \frac{d}{dr} Z_{\rm eff,0}. \tag{8}$$

As a consequence of the electrostatic approximation, Ohm's law (Eq. (5)) has been linearized. Therefore, the current perturbation $\tilde{J}_z$ can now be eliminated from Eq. (6), yielding three nonlinear equations for ϕ, $\tilde{\eta}_{\rm sp}$, and $\tilde{Z}_{\rm eff}$.

$$\frac{\rho_m}{B_z^2} \frac{d}{dt} \nabla_\perp^2 \phi = -\frac{1}{\eta_0} \nabla_\parallel^{(0)^2} \phi - \frac{J_{z0}}{B_z} \nabla_\parallel^{(0)} \left(\frac{\tilde{\eta}}{\eta_0} \right), \tag{9}$$

$$\frac{d}{dt} \tilde{\eta}_{\rm sp} - \chi_T \nabla_\parallel^{(0)^2} \tilde{\eta}_{\rm sp} = -\frac{1}{r} \frac{\partial \phi}{\partial \theta} \frac{d\eta_{\rm sp,0}}{dr}, \tag{10}$$

$$\frac{d}{dt}\tilde{Z}_{\rm eff} - \chi_z \nabla_{\parallel}^{(0)^2} \tilde{Z}_{\rm eff} = -\frac{1}{r}\frac{\partial \phi}{\partial \theta}\frac{d}{dr} Z_{\rm eff,0}. \tag{11}$$

Equations (9), (10) and (11), for the vorticity, Spitzer resistivity, and impurity density evolution, constitute the basic resistivity-gradient-driven turbulence model to be used in the analytic calculations.

III. Linear Theory

In this section, the linear instability described by Eqs. (9)-(11) is studied in detail. This system of equations reduces, in the linear approximation, to a single second-order equation,

$$\frac{d^2}{dx^2}\phi - \left(\frac{1}{4}x^2 - \frac{\delta_T x}{1+b_T x^2} - \frac{\delta_z x}{1+b_z x^2}\right)\phi = 0. \tag{12}$$

$x = \dfrac{r-r_s}{x_R}$ is the dimensionless radial variable and x_R is the resistive singular layer width, where

$$x_R = \left[\gamma\left(\frac{\mu_0\rho_m}{B_z^2}\right)\frac{\eta_0(r_s)}{\mu_0}\frac{L_s^2 r_s^2}{4m^2}\right]^{1/4},$$

$$\delta_T = \frac{L_s}{L_\eta}\frac{\eta_0 J_{z0}}{B_z}\bigg|_{rs}\frac{1}{4\gamma x_R},$$

$$\delta_z = \frac{L_s}{L_z}\frac{\eta_0 J_{z0}}{B_z}\bigg|_{rs}\frac{1}{4\gamma x_R},$$

$$b_T = \frac{m^2}{r_s^2 L_s^2}\chi_T\frac{x_R^2}{\gamma},$$

$$b_z = \frac{m^2}{r_s^2 L_s^2}\chi_z\frac{x_R^2}{\gamma}.$$

Here, $L_\eta = [d\ell n\eta_{\rm sp}/dr]^{-1}$ and $L_z = [d\ell n Z_{\rm eff}/dr]^{-1}$ are the gradient-scale lengths of the Spitzer resistivity and the impurity, and $L_s = R_0 q^2/r_s q'$ is the magnetic shear scale length. A key dimensionless ratio is $S = \tau_R/\tau_{Hp}$, where $\tau_R = \mu_0 a^2/\eta_0$ is the resistive diffusion time, and $\tau_{Hp} = R_0/V_A$ is the poloidal hydromagnetic time with $V_A = B_z/(\mu_0\rho_m)^{1/2}$ the Alfvén speed. Here R_0, a, r_s, and m denote major radius, minor radius, radial location of singular layer, safety factor, and poloidal wave number, respectively. The first term in Eq. (12) represents inertia and the second represents field line bending. The last two terms describe the instability driving force (δ_T and δ_z) reduced by the relevant transport effects

(b_T and b_z). We note that δ_T and δ_z are proportional to the Spitzer resistivity and $Z_{\rm eff}$ gradients respectively, while b_T and b_z are proportional to χ_T and χ_z. Therefore, the clean hydrogenic plasma model corresponds to $\delta_z = 0$, and the isothermal plasma to $\delta_T = 0$ and $b_T = \infty$.

In the absence of an impurity species, Eq. (12) has been studied in detail in Ref. (13). There it was shown that in the limit of no thermal conduction, the growth rate is given by[12]

$$\gamma = \left(\frac{Sma^3 R_0 L_s}{4 r_s L_\eta^2}\right)^{2/5} \left(\frac{\mu_0 J_{z0}(r_s)}{B_z}\right)^{4/5} \tau_R^{-1} \propto \eta_0^{3/5}. \tag{13}$$

In the large thermal conduction limit, the growth rate is greatly reduced, and is given by[12]

$$\gamma = 1.34 \frac{S^2 R_0^2}{a^2} \left(\frac{L_s^3 r_s}{L_\eta^2 m}\right)^{2/3} \left(\frac{\mu_0 J_{z0}(r_s)}{B_z}\right)^{4/3} \left(\frac{\eta_0(r_s)}{\mu_0 \chi_T}\right)^{4/3} \tau_R^{-1} \propto \frac{\eta_0^{1/3}}{\chi_T^{4/3}}. \tag{14}$$

We note that the parallel electron thermal conduction does not completely stabilize the rippling mode because this effect is negligible near x=0, as easily seen in Eq. (12). Since most discharges of large present day tokamaks are characterized by relatively high temperature, Eq. (14) is more appropriate than Eq. (13), even near the edge.

The linear growth rates predicted by Eq. (14) are already quite small, and the inclusion of electron kinetic effects tend to stabilize the mode. For these reasons, rippling modes have been ignored except in the context of edge physics. However, as proposed by Rutherford, rippling modes driven by $Z_{\rm eff}$-gradients can be unstable with large growth rates even in the case when parallel electron conduction is large.[14] In contrast to the rippling mode in clean plasmas (driven by temperature-gradient), the impurity driven rippling mode is quite insensitive to stabilizing electron kinetic effects because the $Z_{\rm eff}$-evolution is governed by ion dynamics rather than electron dynamics.

Rutherford considered the isothermal limit ($\delta_z \neq 0$, $b_T \to \infty$), in which case Eq. (12) can be simplified to

$$\frac{d^2}{dx^2}\phi - \left(\frac{1}{4}x^2 - \frac{\delta_z x}{1 + b_z x^2}\right)\phi = 0. \tag{15}$$

Equation (15) has the same mathematical structure as the case of the clean plasma ($\delta_z = 0$) case. Therefore, the linear growth rate for $b_z \ll 1$ is given by

$$\gamma = \left(\frac{Sma^3 R_0 L_s}{4 r_s L_z^2}\right)^{2/5} \left(\frac{\mu_0 J_{z0}(r_s)}{B_z}\right)^{4/5} \tau_R^{-1}. \tag{16}$$

For $b_z \gg 1$,

$$\gamma = 1.34 \frac{S^2 R_0^2}{a^2} \left(\frac{L_s^3 r_s}{L_z^2 m} \right)^{2/3} \left(\frac{\mu_0 J_{z0}(r_s)}{B_z} \right)^{3/4} \left(\frac{\eta_0(r_s)}{\mu_0 \chi_z} \right)^{4/3} \tau_R^{-1}. \quad (17)$$

The isothermal model demonstrates the robustness of the impurity gradient driven rippling instability, even in a relatively high temperature regime. However, it is somewhat oversimplified, and fails to describe interesting features which are related to the relative sign of the Spitzer resistivity and Z_{eff} gradients. When there is only one driving term (either $\delta_z = 0$ or $\delta_T = 0$), the growth rate does not depend on the sign of δ (only on the magnitude). But in general, when both driving terms are present, the growth rate can be significantly reduced if the Spitzer resistivity and impurity concentration have opposite gradients. In order to study this effect, linear growth rates have been obtained numerically from the initial value code 'KITE'[17] which is described in Sec. IV. We consider the m=20, n=8 mode with typical Macrotor edge parameters. The results are summarized in Figs. 1, 2 and 3.

In Fig. 1, linear growth rates are plotted as a function of L_z for $L_\eta \cong 0.32a$ and various values of χ_T (and $\chi_z \cong 0.025\chi_T$). Growth rates for $L_z > 0$ are larger than those for $L_z < 0$. The condition $L_z > 0$ implies that Z_{eff} is peaked at the edge, so that the gradients in Z_{eff} and η_{sp} have like sign. This important feature, which is not accounted for in the isothermal model, manifests the sensitivity of the instability dynamics to the Z_{eff} profile. Figure 2 demonstrates close agreement between results from the initial value code and those of the shooting code described below. The shooting results show the crossing of eigenvalues at $L_z^{-1}a \cong -2.3$, which yields the minimum growth rate of the most unstable mode. The structures of the electrostatic potential eigenfunction and the effective potential of Eq. (12) for three different values of L_z^{-1} are plotted in Fig. 3. For $L_z^{-1}a > -2.3$, the eigenmodes with electrostatic potential ϕ peaked outside the rational surface are more unstable than those with ϕ peaked inside the rational surface. On the other hand, for $L_z^{-1}a < -2.3$, the eigenmodes with ϕ peaked inside the rational surface are most unstable. At $L_z^{-1}a \cong -2.3$, two branches of eigenmodes are degenerate thus yielding the same growth rate. Typical eigenmode structures for the most unstable modes as obtained from the initial value code are plotted in Fig. 4. It is apparent from the

figures that ϕ, $\tilde{T}$, and $\tilde{Z}_{\rm eff}$ are peaked away from the mode rational surface, in contrast to the current perturbation which peaks at the rational surface. As is characteristic of resistivity-gradient-driven turbulence,[11] the ϕ, $\tilde{T}$, and $\tilde{Z}_{\rm eff}$ profiles are further shifted away from rational surface as the fluctuation level increases. Consequently, the potential, Spitzer resistivity, and $\tilde{Z}_{\rm eff}$ perturbation effectively 'decouple' from the current perturbation. This decoupling allows considerable simplification in the theoretical description of the nonlinear saturated state, as we shall see in the following section.

IV. Nonlinear Theory

In this section, an analytical theory of the nonlinear evolution and saturation of impurity-gradient-driven turbulence is presented. The nonlinear saturation mechanism is identified and the levels of turbulent impurity and thermal diffusion at saturation are calculated. We consider dynamical turbulent saturation for a finite-gradient resistivity profile, rather than saturation by quasilinear flattening of the background resistivity gradients. This is a natural assumption for tokamaks, because the temperature (impurity) profile is maintained by the competition of plasma heating (impurity source) and transport. This assumption is further justified by the robustness of the saturation mechanism we consider. It consists of turbulent diffusion-induced broadening of the resistivity perturbation which efficiently couples to the impurity drag on the ions. This saturation mechanism persists in the presence of quasilinear flattening of the background resistivity gradient and may reasonably be assumed to dominate quasilinear relaxation.[11]

In a previous investigation,[11] the saturation of resistivity-gradient-driven turbulence was specified by the time-stationarity of energy-like integrals quadratic in the fluctuation levels. This specification also provides useful insight in the present case. The relevant energy-like quantities are:

$$E_k = 1/2 \int d^3x |\nabla_\perp \phi|^2,$$

$$E_T = 1/2 \int d^3x |\tilde{\eta}_{\rm sp}|^2,$$

$$E_z = 1/2 \int d^3x |\tilde{Z}_{\rm eff}|^2.$$

From Eqs. (9)-(11), it can be shown that E_k, E_T, and E_z evolve according to:

$$\frac{\partial E_k}{\partial t} = \frac{B_z^2}{\rho_m} \int d^3x \left[\frac{\phi^* J_{z0}}{B_z} \nabla_\parallel^{(0)} \left(\frac{\tilde{\eta}}{\eta_0} \right) - \frac{|\nabla_\parallel^{(0)} \phi|^2}{\eta_0} \right], \tag{18}$$

$$\frac{\partial E_T}{\partial t} = \int d^3x \left[-\tilde{\eta}_{\rm sp}^* \frac{1}{r} \frac{\partial \phi}{\partial \theta} \frac{d}{dr} \eta_{\rm sp,0} - \chi_T \left| \nabla_\parallel^{(0)} \tilde{\eta}_{\rm sp} \right|^2 \right], \tag{19}$$

$$\frac{\partial E_z}{\partial t} = \int d^3x \left[-\tilde{Z}_{\rm eff}^* \frac{1}{r} \frac{\partial \phi}{\partial \theta} \frac{d}{dr} \tilde{Z}_{\rm eff} - \chi_z \left| \nabla_\parallel^{(0)} \tilde{Z}_{\rm eff} \right|^2 \right]. \tag{20}$$

Equation (18) states that the fluid kinetic energy evolves by competition between a destabilizing $\vec{J} \times \vec{B}$ force induced by resistivity perturbations and a stabilizing $\vec{J} \times \vec{B}$ force induced by the magnetic field line diffusion. Equation (19) states that the mean-square Spitzer resistivity fluctuation level is driven by relaxation of the average gradient (note that $\langle (\tilde{\eta}_{\rm sp}/r)(\partial\phi/\partial\theta) \rangle$ is the average radial Spitzer resistivity flux) and damped by dissipation due to χ_T. The evolution of mean-square $Z_{\rm eff}$ fluctuation level is similar to that of the Spitzer resistivity fluctuation level. Clearly, in the turbulent steady state, the energy-like quantities E_k, E_T, and E_z are stationary in time. It should be noted that requiring $\frac{\partial}{\partial t} E_k = 0$ is equivalent to imposing

$$\int d^3x \phi^* \nabla_\parallel^{(0)} \tilde{J}_z = 0.$$

A sufficient condition for satisfaction of this criterion is $\tilde{J}_z = 0$. This condition is satisfied as the turbulence evolves nonlinearly so that the resistivity and potential perturbations shift away from the rational surface where the current perturbation is localized. Thus $\tilde{J}_z$ is approximately zero in the region of interest. Consequently, the vorticity equation decouples from the evolution equations for $\eta_{\rm sp}$ and $Z_{\rm eff}$. Furthermore, Ohm's law with $\tilde{J}_z$=0 provides a simple relationship between ϕ, $\eta_{\rm sp}$ and $Z_{\rm eff}$, so that steady state impurity driven turbulence is described by $\eta_{\rm sp}$ and $Z_{\rm eff}$ evolution. Time stationarity of the remaining energies, E_T and E_z, is satisfied as the widths of the resistivity and potential fluctuations broaden to the point where parallel heat conduction $\chi_T \nabla_\parallel^{(0)^2}$ and impurity ion drag, $\chi_z \nabla_\parallel^{(0)^2}$ balance the Spitzer resistivity gradient and $Z_{\rm eff}$ gradient sources. The

broadening of the resistivity and potential perturbations results from nonlinear convection and grows in magnitude as the fluctuation amplitudes increase. The degree of broadening, i.e., the radial scale of the fluctuations, at any given fluctuation level, is determined from renormalized evolution equations for $\eta_{\rm sp}$ and $Z_{\rm eff}$.

To obtain the renormalized evolution equations we use a standard iterative method.[11] Renormalization is performed by substituting for $\tilde{\eta}_{{\rm sp},\vec{k}''}$ and $\tilde{Z}_{{\rm eff},\vec{k}''}$ the terms $\tilde{\eta}^{(2)}_{{\rm sp},\vec{k}''}$ and $\tilde{Z}^{(2)}_{{\rm eff},\vec{k}''}$ which are driven by the direct beat of the test ($\vec{k}$) and background ($\vec{k}'$) modes. Following previous investigations of resistivity-gradient-driven turbulence,[11] we neglect $\phi^{(2)\prime\prime}_{\vec{k}}$. Using the symmetries, $\tilde{\eta}_{{\rm sp},-\vec{k}} = \tilde{\eta}_{{\rm sp},\vec{k}}$, $\tilde{Z}_{{\rm eff},-\vec{k}} = \tilde{Z}_{{\rm eff},\vec{k}}$, and $\phi_{-\vec{k}} = \phi_{\vec{k}}$, and retaining only the (dominant) radial diffusion term, we obtain the renormalized resistivity equations,

$$\frac{\partial}{\partial t}\tilde{\eta}_{{\rm sp},\vec{k}} + \chi_T k_\parallel^2 \tilde{\eta}_{{\rm sp},\vec{k}} - D^T_{\vec{k}} \frac{\partial^2}{\partial x^2}\tilde{\eta}_{{\rm sp},\vec{k}} = -ik_\theta \phi_{\vec{k}} \frac{d\eta_0}{dr}, \tag{21}$$

$$\frac{\partial}{\partial t}\tilde{Z}_{{\rm eff},\vec{k}} + \chi_Z k_\parallel^2 \tilde{Z}_{{\rm eff},\vec{k}} - D^z_{\vec{k}} \frac{\partial^2}{\partial x^2}\tilde{Z}_{{\rm eff},\vec{k}} = -ik_\theta \phi_{\vec{k}} \frac{dZ_{{\rm eff},0}}{dr}, \tag{22}$$

where

$$D^T_{\vec{k}} = \sum_{\vec{k}'} k'^2_\theta |\phi_{\vec{k}'}|^2 \left[\gamma_{\vec{k}+\vec{k}'} + \chi_T (k_\parallel + k'_\parallel)^2\right]^{-1}, \tag{23}$$

$$D^z_{\vec{k}} = \sum_{\vec{k}'} k'^2_\theta |\phi_{\vec{k}'}|^2 \left[\gamma_{\vec{k}+\vec{k}'} + \chi_z (k_\parallel + k'_\parallel)^2\right]^{-1}, \tag{24}$$

Here, the diffusion coefficients $D^T_{\vec{k}}$ and $D^z_{\vec{k}}$ represent the crucial nonlinear effect of random convection of resistivity by fluid turbulence.

The natural radial scales for turbulent resistivity fluctuations in the saturated state are determined by the asymptotic balance of thermal conduction or impurity-ion drag with the turbulent diffusion. From Eqs. (21) and (22), these scales are found to be

$$\Delta^T_{\rm k} = (D^T_{\rm k}/\chi_T k'^2_\parallel)^{1/4} \tag{25}$$

and

$$\Delta^z_{\rm k} = (D^z_{\rm k}/\chi_z k'^2_\parallel)^{1/4} \tag{26}$$

where $k_\parallel = k'_\parallel x$. Note that the radial scales $\Delta^T_{\rm k}$ and $\Delta^z_{\rm k}$ are amplitude dependent through the potential fluctuation amplitude dependence of the $D_{\rm k}$'s. Hence, in the nonlinear

regime, the basic radial scales are determined not by the linear eigenmode width, but by the turbulent correlation lengths. To explicitly express the potential fluctuation amplitude dependence in terms of $\Delta^T_{\mathbf{k}}$ and $\Delta^z_{\mathbf{k}}$, we substitute for $D^T_{\mathbf{k}}$ and $D^z_{\mathbf{k}}$ in Eqs. (25) and (26), using Eqs. (23) and (24). We first, however, simplify Eqs. (23) and (24) by using a Markovian approximation in the resistivity response functions, so that we can write:

$$D^T \approx \frac{\langle \hat{v}_r^2 \rangle}{\chi_T \bar{k}_\parallel'^2 (\Delta^T)^2} \tag{27}$$

$$D^z \approx \frac{\langle \hat{v}_r^2 \rangle}{\chi_z \bar{k}_\parallel'^2 (\Delta^z)^2} \tag{28}$$

where $\bar{k}'_\parallel = (k_y)_{\rm rms}/L_s$, $\langle \hat{v}_r^2 \rangle$ is the mean square radial velocity defined by

$$\langle \hat{v}_r^2 \rangle = \sum_k k_\theta^2 |\phi_k^2|, \tag{29}$$

and Δ^T and Δ^z are evaluated using $\bar{k}$. Substituting Eqs. (27) and (28) into Eqs. (25) and (26) then yields

$$(\Delta^T)^3 = \langle \hat{v}_r^2 \rangle^{1/2} / \chi_T \bar{k}_\parallel'^2 \tag{30}$$

and

$$(\Delta^z)^3 = \langle \hat{v}_r^2 \rangle^{1/2} / \chi_z \bar{k}_\parallel'^2 \tag{31}$$

where $k'_\parallel$ is evaluated at $\bar{k}'_\parallel$. It is clear that the nonlinearly saturated state, characterized by these nonlinear scales Δ^T and Δ^z, and the condition $\tilde{J}_z$=0, is radically different in character from the linear regime.

We now determine $\langle \hat{v}_r^2 \rangle$ at saturation. Using Ohm's law with $\tilde{J}_z$=0 in order to eliminate ϕ, the renormalized resistivity evolution equations in the steady state are given by

$$\left(\chi_T k_\parallel'^2 x^2 - D^T_{\vec{k}} \frac{\partial^2}{\partial x^2} \right) \tilde{\eta}_{{\rm sp},\vec{k}} = \frac{L_s E_0}{L_\eta B_z x} \left(\tilde{\eta}_{{\rm sp},\vec{k}} + \frac{\eta_{\rm sp.0}}{Z_{\rm eff.0}} \tilde{Z}_{{\rm eff},\vec{k}} \right), \tag{32}$$

and

$$\left(\chi_Z k_\parallel'^2 x^2 - D^z_{\vec{k}} \frac{\partial^2}{\partial x^2} \right) \tilde{Z}_{{\rm eff},\vec{k}} = \frac{L_s E_0}{L_z B_z x} \left(\tilde{Z}_{{\rm eff},\vec{k}} + \frac{Z_{\rm eff.0}}{\eta_{\rm sp.0}} \tilde{\eta}_{{\rm sp},\vec{k}} \right), \tag{33}$$

where $E_0 = \eta_{\rm sp.0} Z_{\rm eff.0} J_{z_0}$. The content of Eqs. (32) and (33) is essentially equivalent to that of requiring time stationarity of the energy integrals E_T and E_z, i.e., that saturation

represents the dynamically regulated balance between Spitzer resistivity gradient drive (or $Z_{\rm eff}$-gradient drive) and the radially dependent parallel thermal conduction (or impurity drag on ion flow). To determine fluctuation levels at saturation, Eqs. (32) and (33) can be multiplied by $\tilde{Z}^*_{\rm eff}$ and integrated over x in order to yield a closed set of coupled algebraic equations for the quantities $\int dx \tilde{Z}^*_{\rm eff}\tilde{\eta}_{\rm sp}$ and $\int dx|\tilde{Z}_{\rm eff}|^2$. This procedure for specifying saturation, while equivalent to the conditions $\partial E_T/\partial t = \partial E_z/\partial t = 0$, is preferable since it yields closed equations. The conditions $\partial E_T/\partial t = \partial E_z/\partial t = 0$, on the other hand, gives two equations with three unknown quantities, $\int dx|\tilde{\eta}_{\rm sp}|^2$, $\int dx|\tilde{Z}_{\rm eff}|^2$, and $\int dx\tilde{\eta}_{\rm sp}\tilde{Z}^*_{\rm eff}$. The two coupled equations obtained from Eqs. (32) and (33) are

$$\langle Z|\mathcal{L}^T|\eta\rangle\langle Z|\eta\rangle - \frac{L_s E_0}{L_\eta B_z}\frac{\eta_{\rm sp.0}}{Z_{\rm eff.0}}\left\langle Z\left|\frac{1}{x}\right|Z\right\rangle\langle Z|Z\rangle = 0, \tag{34}$$

$$\langle Z|\mathcal{L}^z|Z\rangle\langle Z|Z\rangle - \frac{L_s E_0}{L_z B_z}\frac{Z_{\rm eff.0}}{\eta_{\rm sp.0}}\left\langle Z\left|\frac{1}{x}\right|\eta\right\rangle\langle Z|\eta\rangle = 0, \tag{35}$$

where

$$\mathcal{L}^T = \chi_T {k'_\parallel}^2 x^2 - D^T_{\tilde{k}}\frac{\partial^2}{\partial x^2} - \frac{L_s E_0}{L_\eta B_z}\frac{1}{x},$$

$$\mathcal{L}^z = \chi_z {k'_\parallel}^2 x^2 - D^z_{\tilde{k}}\frac{\partial^2}{\partial x^2} - \frac{L_s E_0}{L_z B_z}\frac{Z_{\rm eff.0}}{\eta_{\rm sp.0}}\frac{1}{x},$$

and

$$\langle a|Q|b\rangle \equiv \int_{-\infty}^{\infty} dx\ a^* Q b \Big/ \int_{-\infty}^{\infty} dx\ a^* b,$$

$$\langle a|b\rangle \equiv \int_{-\infty}^{\infty} dx\ a^* b.$$

In order to have a non-trivial solution of Eqs. (34) and (35), it is necessary that

$$\left\| \begin{array}{cc} \langle Z|\mathcal{L}^T|\eta\rangle, & -\dfrac{L_s E_0}{L_\eta B_z}\dfrac{\eta_{\rm sp.0}}{Z_{\rm eff.0}}\left\langle Z\left|\dfrac{1}{x}\right|Z\right\rangle \\ -\dfrac{L_s E_0}{L_z B_z}\dfrac{Z_{\rm eff.0}}{\eta_{\rm sp.0}}\left\langle Z\left|\dfrac{1}{x}\right|\eta\right\rangle, & \langle Z|\mathcal{L}^z|Z\rangle \end{array} \right\| = 0, \tag{36}$$

We have previously noted the asymmetric nature of the mode structure of the resistivity fluctuations $\tilde{\eta}_{\rm sp}$ and $\tilde{Z}_{\rm eff}$. This asymmetry, present in the linear phase, is further developed in the saturated state where decoupling occurs. The asymmetry is responsible

for maintaining the energy input from the gradients since, for radial eigenfunctions of even parity, the source terms in Eq. (36) would vanish. As a consequence, the region $x \approx 0$ is irrelevant in the integrals of Eq. (36), even for the integrand of $\left\langle Z \left| \frac{1}{x} \right| \eta \right\rangle$ which remains small near x=0. The matrix elements in Eq. (36) all reduce to moments of the wave functions $\tilde{Z}_{\text{eff}}$ and $\tilde{\eta}_{\text{sp}}$ with respect to various powers of x. The wave functions have well defined widths, so that the moments yield appropriate powers of the mixing lengths Δ^T and Δ^z. When the integral involves the product of wave functions $\tilde{Z}_{\text{eff}}$ and $\tilde{\eta}$, the smaller of the two widths Δ^z and Δ^T determines the overall width. From Eqs. (30) and (31) and the fact that $\chi_T \gg \chi_z$, we note that $\Delta^T < \Delta^z$. We also substitute for the diffusion coefficients D^T and D^z in terms of the widths Δ^T and Δ^z using Eqs. (25) and (26). Following this procedure yields

$$\left\| \begin{array}{cc} \chi_T k_\parallel'^2 (\Delta^T)^2 - \dfrac{E_0 L_s}{B_z L_\eta \Delta^T}, & -\dfrac{E_0 L_s}{B_z L_\eta} \dfrac{\eta_{\text{sp},0}}{Z_{\text{eff},0}} \dfrac{1}{\Delta^z} \\ -\dfrac{E_0 L_s}{B_z L_z} \dfrac{Z_{\text{eff},0}}{\eta_{\text{sp},0}} \dfrac{1}{\Delta^T}, & \chi_z k_\parallel'^2 (\Delta^z)^2 - \dfrac{E_0 L_s}{B_z L_z} \dfrac{1}{\Delta^z} \end{array} \right\| = 0, \tag{37}$$

Substituting for Δ^T and Δ^z from Eqs. (30) and (31), and evaluating the determinant yields the saturation condition

$$\left\langle \hat{v}_r^2 \right\rangle^{1/2} = \frac{L_s}{L_\eta} \frac{E_0}{B_z} (1 + \eta_z), \tag{38}$$

where

$$\eta_z = \frac{L_\eta}{L_z}.$$

The mean square radial velocity exhibits the predictable scaling with respect to the magnetic shear scale length and the scale length of the driving gradient. Because two gradients drive the turbulence, Eq. (38) includes both L_s/L_η and L_s/L_z terms. Furthermore, due to the asymmetric nature of impurity gradient driven turbulence, the relative direction of the gradients has a strong effect on the fluctuation level.

To obtain expressions for the turbulent diffusion coefficients of Spitzer resistivity and Z_{eff}, we combine Eqs. (27), (28), (30), (31), and (38), yielding

$$D_{\tilde{k}}^T \approx \left[\frac{E_0 L_s}{B_z L_\eta} (1 + \eta_z) \right]^{4/3} \Big/ (\chi_T k_\parallel'^2)^{1/3}, \tag{39}$$

and

$$D_{\vec{k}}^{z} \approx \left[\frac{E_0 L_s}{B_z L_\eta}(1+\eta_z)\right]^{4/3} \Big/ (\chi_z k_\parallel'^2)^{1/3}. \tag{40}$$

We observe that the turbulent diffusion coefficients are only weakly dependent upon χ_T (or χ_z). This contrasts sharply with intuition based on linear growth rates and linear eigenmode widths $\left(D \sim \frac{\gamma}{k_\perp^2}\right)$ which predicts much stronger dependence on $\chi_T(\chi_z)$ and consequently, much lower saturation levels. Also, note that $\left\langle \hat{v}_r^2 \right\rangle^{1/2} = (L_s E_0 / L_\eta B_z)(1+\eta_z)$ and that since $D \sim \chi^{-1/3}$, $D^z/D^T \sim (\chi_T/\chi_z)^{1/3} \sim (m_i/m_e)^{1/6}$. Hence, the insensitivity of the saturation level to parallel transport parameters is also manifested by the relatively modest increase in $\left\langle \hat{v}_r^2 \right\rangle^{1/2}$ and D^T when impurity dynamics are taken into account ($\eta_z \neq 0$), as well as by the relation $D^z/D^T \sim (m_i/m_e)^{1/6}$. Thus, the principal consequences of retaining impurity dynamics are an increase in the domain of linear instability and the possibility of meaningful estimates of density mixing lengths and fluctuation levels.

After the completion and presentation[17] of the results of this study of the coupled thermal, Z_{eff}-gradient driven problem, an alternative derivation of the results for each individual cases was proposed by Connor.[18]. In that work, Connor derived a 'scaling' of $m_{\text{rms}} \sim \chi_T^{-5/4}$ (root-mean-squared value of poloidal wavenumber) using invariance techniques. By way of comparison, we treated m_{rms} as a number in Ref. 11 and Ref. 17 (note that the only direct comparisons possible are with Ref. 11, which dealt with the pure thermal case). This difference then propagates through all predictions of transport scalings, fluctuation levels, etc. We feel our approach is superior for the following reasons. First, Connor's scaling applies only to a narrow range of χ_T values. Second, Connor's dimensional analysis omits important physics considerations, such as the applicability of current decoupling ($\tilde{J}_z \cong 0$ in growth region), which requires

$$\chi_T < \frac{R_0^2}{\tau_R} S^2 \left(\frac{\Delta^T}{a}\right)^2 \frac{\eta_0(r_s)}{\eta_0(0)} \frac{\rho_m(r_s)}{\rho_m(0)},$$

and the restrictions imposed by the inequality $\partial/\partial x > k_\theta$, which requires

$$m_{\text{rms}} < \left(\frac{\hat{s}}{q}\right)^2 \chi_T \frac{r_0}{R_0^2} \frac{L_\eta B_z}{L_s E_0}.$$

Indeed, Connor overlooked the possibility that the inequality $\partial/\partial x < k_\theta$ is violated for larger m. Both of these considerations strongly bound the range of variation of m_{rms} from

below and above, and make 'scalings' of $m_{\rm rms}$ rather dubious. Furthermore, numerical results and detailed analysis[19] indicate that $m_{\rm rms}$ is nearly insensitive to parameter variation and scaling. Hence, we feel that the most physical approach is to leave $m_{\rm rms}$ as a parameter.

We have studied three dimensional multiple helicity-impurity-gradient-driven turbulence numerically in order to test the analytical results derived in this section. The initial value code KITE[20] which has been used for the resistivity-gradient-driven turbulence[11] has been modified to incorporate the $Z_{\rm eff}$ evolution (Eq. (8)). Details regarding the numerical scheme used in this code and the convergence studies for resistivity-gradient-driven turbulence calculations are discussed in Ref. 20. In this work, we consider a cylindrical tokamak equilibrium with the electron temperature profile,

$$T_e(r) = T_e(0)\left(1+\left(\frac{r}{r_0}\right)^2\right)^{-4/3}, \tag{41}$$

where $r_0 = 0.63$, and an equilibrium current profile,

$$J_{z0}(r) = -\frac{B_z}{\mu_0 R_0}\frac{2}{q(0)}\left(\frac{T_e(r)}{T_e(0)}\right)^{3/2}\frac{Z_{\rm eff}(0)}{Z_{\rm eff}(r)}, \tag{42}$$

where $q(0) = 1$. Profiles for T_e, $Z_{\rm eff}$, total resistivity, and q are plotted in Fig. 5 for three different values of L_z. It is apparent that changes in the q profile arising from $Z_{\rm eff}$ profile changes are small.

The numerical calculations have been performed in the same way as described in Ref. 20. An annular region around the singular surface of the 5/2 resonance has been considered. The width of this annular region in radius is approximately $0.40a$ and the radial grid spacing used is $\Delta r = 1.8\cdot 10^{-3}a$. In Fig. 6, we have plotted the time averaged mean square radial velocity level at saturation as a function of radius for three different values of L_z, and compared it to the analytical results given by Eq. (38). As discussed in Ref. 11, the value of $\bar{E}$ given in the figure does not include the contribution of the resonant helicity (test) mode at the corresponding radial location. The rather strong dependence of $\bar{E}$ on $\eta_z = \left(\frac{L_\eta}{L_z}\right)$, as predicted by Eq. (38), is clearly shown in Fig. 6.

The agreement of numerical results with analytical prediction is very good for the cases where $L_z = -0.65a$ and $L_z = \infty$. For $L_z = 0.91a$ the analytical prediction is

lower approximately by a factor of two. In this case, a large value of the saturated kinetic energy, and the resulting increase in the Reynolds number imply the need for higher spatial resolution. Hence, a broader m spectrum is required to represent the turbulent state at saturation. For this reason, limitations on present computing capabilities make it difficult to study cases with impurity density profiles sharply peaked at the edge. Nevertheless, the predicted scaling of $\bar{E}$ with the effective gradient $(1+\eta_z)/L_\eta$ is in good, semi-quantitative agreement with the results of numerical calculations. Note that this study also constitutes a further, more general test of the basic resistivity-gradient-driven turbulence model.

V. Fluctuation Levels and Anomalous Transport Coefficients

In the previous section, the basic nonlinear spatial and temporal scales (mixing lengths and correlation times) which characterize impurity gradient driven turbulence were identified and used to determine saturated turbulence levels. In this section, analytical expressions for the temperature $\tilde{T}/T_0$, density $\tilde{n}/n_0$, and potential fluctuation levels are derived and used to calculate electrostatic convective particle and thermal diffusivities. The related magnetic fluctuation levels and the associated thermal conductivity are also estimated. The results compare quite favorably with several experimental observations from tokamak edge plasmas.

Temperature fluctuation evolution is determined by Eq. (21), so that

$$\left(\frac{\tilde{T}}{T_0}\right)_{\mathbf{k}} \approx \left(\chi_T k_\parallel'^2 \Delta_{\mathbf{k}}^{T^2}\right)^{-1} \frac{\hat{v}_{r\mathbf{k}}}{L_T} \tag{43}$$

and, from Eqs. (27), (30) and (38),

$$\left(\frac{\tilde{T}}{T_0}\right)_{\mathrm{rms}} \approx \frac{\Delta_{\mathbf{k}}^T}{L_T} \approx \frac{1}{L_T}\left(\frac{L_s}{L_\eta}\frac{E_0}{B_z}(1+\eta_z)\right)^{1/3} (\chi_T \bar{k}_\parallel'^2)^{-1/3}. \tag{44}$$

Note that the effective turbulent mixing length for temperature fluctuations is $\Delta_{\mathbf{k}}^T$, the thermal conduction layer width determined by parallel and radial diffusion.

Similarly, ion density evolution is governed by the continuity equation, Eq. (A1), where the compression term is determined by the balance of the parallel ion pressure gradient with ion-impurity friction. Thus, $\hat{v}_\parallel \cong -\chi_z \nabla_\parallel^{(0)}(\tilde{n}/n_0)$. Hence, noting that

$\tilde{J}_z \sim 0$ follows from decoupling, density fluctuations evolve according to

$$\left(\frac{d}{dt} - \chi_z \nabla_{\parallel}^{(0)^2}\right) \frac{\tilde{n}}{n_0} = -\hat{v}_{r_{\mathbf{k}}} \left(\frac{1}{n_0}\frac{dn_0}{dr}\right), \tag{45}$$

so that Δ^z is the characteristic spatial scale for density fluctuations. Hence,

$$\left(\frac{\tilde{n}}{n_0}\right)_{\mathbf{k}} \approx \left(\chi_z k_{\parallel}'^2 \Delta_{\mathbf{k}}^{z^2}\right)^{-1} \frac{\hat{v}_{r_{\mathbf{k}}}}{L_n}, \tag{46}$$

where $L_n^{-1} = -(1/n_0)(dn_0/dr)$ is the density gradient scale length. Using Eqs. (28), (31) and (38), it follows that

$$\left(\frac{\tilde{n}}{n_0}\right)_{\text{rms}} \approx \frac{\Delta_{\mathbf{k}}^z}{L_n} = \frac{1}{L_n}\left(\frac{L_s}{L_\eta}\frac{E_0}{B_z}(1+\eta_z)\right)^{1/3} (\chi_z \bar{k}_{\parallel}'^2)^{-1/3}. \tag{47}$$

Note that the effective turbulent mixing length for density fluctuations is Δ^z. Since $\chi_T \gg \chi_z$, it follows from Eqs. (30) and (31) that $\Delta^z > \Delta^T$ and hence that $(\tilde{n}/n_0)_{\text{rms}} > (\tilde{T}/T_0)_{\text{rms}}$, for $L_n \sim L_T$. Thus, the disparity between the density and temperature correlation lengths Δ^z, Δ^T can reconcile the resistivity-gradient-driven turbulence model with the experimental observation[3,4] that $(\tilde{n}/n_0)_{\text{rms}} > (\tilde{T}/T_0)_{\text{rms}}$. Finally, note that Eq. (47) corrects and supercedes the density fluctuation level estimate given by Eq. (26) of Ref. 11.

The potential fluctuation level can be easily calculated using Eq. (38). It follows directly that

$$\left(\frac{e\hat{\Phi}}{T_0}\right)_{\text{rms}} \approx \frac{\left[\langle \hat{v}_r^2 \rangle\right]^{1/2}}{\bar{k}_\theta \rho_s c_s} = \left(\frac{E_0 L_s}{B_z L_\eta}\right) \frac{(1+\eta_z)}{(\bar{k}_\theta \rho_s c_s)}. \tag{48}$$

Note that unlike the more familiar drift wave turbulence models where $\tilde{n}/n_0 \sim |e|\hat{\Phi}/T_0 \sim 3\rho_s/L_n$,[21] resistivity-gradient-driven turbulence is characterized by the inequality of density and potential fluctuations; i.e., $\tilde{n}/n_0 \neq |e|\hat{\Phi}/T_0$.

In Fig. 7, $(\tilde{n}/n_0)$, $(|e|\hat{\Phi}/T_0)$, and $(\tilde{T}/T_0)$ are plotted as function of radius for Macrotor[22] edge parameters and profiles, with $\eta_z = 0$. In Fig. 8, a similar plot is given, with η_z=1. Note that $e\hat{\Phi}/T$ increases dramatically with η_z. In examining Figs. 7,8 it is useful to recall the parameters scaling of the predicted fluctuation levels, i.e.,

$$\left(\frac{\tilde{n}}{n_0}\right) \sim T^{-5/6} n^{1/3} L_n^{-1} \left(L_\eta^{-1} + L_z^{-1}\right) m_i^{1/6} L_s B_z^{-1/3} V_L^{1/3} \tag{49a}$$

$$\left(\frac{\tilde{T}}{T_0}\right) \sim T^{-5/6} n^{1/3} L_T^{-1} \left(L_\eta^{-1} + L_z^{-1}\right) m_e^{1/6} L_s B_z^{-1/3} V_L^{1/3} \tag{49b}$$

$$\left(\frac{|e|\hat{\Phi}}{T_0}\right) \sim T^{-1} n^0 \left(L_\eta^{-1} + L_z^{-1}\right) L_s V_L, \tag{49c}$$

where $E_0 = V_L/2\pi R$ and $T_e \sim T_i$ in edge plasmas. It is apparent that $(\tilde{n}/n_0) \gg (\tilde{T}/T_0)$ and that $(\tilde{n}/n_0)$ and $(e\hat{\Phi}/T_0)$ have different radial profiles, with $(|e|\hat{\Phi}/T_0)$ increasing more rapidly with radius. In comparing Figs. 7,8 with experimental results, it is worthwhile to note that the roll-over in $\tilde{n}/n$ is due to an increase in L_n, obtained from specific experimental data, at large r/a. Note that the density dependence of $\tilde{n}/n$ is quite weak. Finally, $(\tilde{n}/n_0) \gg 3\rho_s/L_n$, while $\tilde{n}/n_0 \sim 3\rho_s/L_n$ is the typical prediction of drift wave turbulence models.

Several aspects of these results are consistent with data from detailed studies of tokamak edge fluctuations. In particular, the inequality of density and temperature fluctuations, i.e., $\tilde{n}/n_0 > \tilde{T}/T_0$, and the disparity between the radial profiles of $\tilde{n}/n_0$ and $e\hat{\Phi}/T_0$ are frequently observed.[4] The latter observation, and the fact that observed $(\tilde{n}/n_0)$ values frequently exceed $3\rho_s/L_n$, strongly suggest that tokamak edge turbulence is <u>not</u> caused by drift waves, which are consistent with $\tilde{n}/n_0 \sim e\hat{\Phi}/T_0$. However, several experiments indicate that $|e|\hat{\Phi}/T_0 > \tilde{n}/n_0$. Understanding this result remains a challenge, particularly since very large potential fluctuations are observed, i.e., $|e|\hat{\Phi}/T_0 \gtrsim .5$. However, in comparing the profile of $|e|\hat{\Phi}/T$ with experimental results, the possible low frequency effects of MHD activity should be carefully considered. Finally, note that experimental studies of the scaling of $\tilde{n}/n_0$ with B_z and T_e, i.e., I_p with q_L fixed, offer a possible way to distinguish resistivity-gradient-driven turbulence $\left(\tilde{n}/n_0 \sim T^{-5/6} B_z^{-1/3} q\right)$ from drift wave turbulence $\left(\tilde{n}/n_0 \sim T^{1/2} B_z^{-1}\right)$, and to better understand edge fluctuations, in general.

Having obtained the density, temperature and potential fluctuation levels, the convective particle and thermal fluxes and diffusivities can now be calculated straightforwardly. The convective turbulent particle flux Γ_n is given by

$$\Gamma_n = n_0 \left\langle \hat{v}_r (\tilde{n}/n_0) \right\rangle , \tag{50a}$$

and the associated particle diffusivity by

$$D_n = L_n \left\langle \hat{v}_r (\tilde{n}/n_0) \right\rangle . \tag{50b}$$

Thus, using Eqs. (45), (47), (48) and (31), it follows that

$$\Gamma_n = \frac{n_0}{L_n} \left(\frac{E_0}{B_z} \frac{L_s}{L_\eta} (1 + \eta_z) \right)^{4/3} \left(\chi_z \bar{k}_\parallel'^2 \right)^{-1/3} , \tag{51a}$$

and

$$D_n = \left(\frac{E_0}{B_z}\frac{L_s}{L_\eta}(1+\eta_z)\right)^{4/3}\left(\chi_z \bar{k}_\parallel'^2\right)^{-1/3}. \tag{51b}$$

Similarly, the convective turbulent thermal flux Q is given by

$$Q = n_0 T_0 \left(\langle \hat{v}_r(\tilde{n}/n_0)\rangle + \left\langle \hat{v}_r(\tilde{T}/T_0)\right\rangle\right) = T_0\Gamma_n + n_0\Gamma_T \tag{52}$$

where $\Gamma_T \equiv \left\langle \hat{v}_r \tilde{T}\right\rangle$. Using Eqs. (51a), (44), (48), and (30) yields:

$$\begin{aligned} Q &= \frac{n_0 T_0}{L_n}\left(\frac{E_0}{B_z}\frac{L_s}{L_\eta}(1+\eta_z)\right)^{4/3}\left[\left(\chi_z \bar{k}_\parallel'^2\right)^{-1/3} + \eta_e\left(\chi_T \bar{k}_\parallel'^2\right)^{-1/3}\right] \\ &= T_0\Gamma_n\left[1+\eta_e\left(\frac{\chi_z}{\chi_T}\right)^{1/3}\right] \end{aligned} \tag{53}$$

where $\eta_e = L_n/L_T$. Since $(\chi_z/\chi_T) \sim (m_e/m_i)^{1/2}$, $n_0\Gamma_T < T_0\Gamma_n$ for typical values of η_e. Thus $Q \cong T_0\Gamma_n$, so that the thermal flux is due primarily to convection. Note that this result is a consequence of the disparity between density and temperature fluctuation mixing lengths, i.e., $\Delta^z > \Delta^T$, and is consistent with recent results from the Caltech[7] and Tosca[8] tokamaks.

The particle diffusivity $D_n(r)$ given in Eq. (51b) is plotted for Macrotor edge parameters and profiles in Fig. 9. The parameter scalings of D_n are given by:

$$D_n \sim T^{-5/6} n^{1/3}\left(L_\eta^{-1} + L_z^{-1}\right)^{4/3} L_s^2 B_z^{-4/3} V_L^{4/3}. \tag{54}$$

Thus D_n increases as temperature decreases, but is insensitive to density. These trends are manifested in Fig. 9, where $D_n(r)$ increases with radius. Note that $D_n \sim 4\times 10^4 \mathrm{cm}^2/\mathrm{sec}$, and is comparable to Bohm diffusion, but clearly scales differently. In addition, it is instructive to compare Γ_n as given by Eq. (51a) with that given in Eq. (95) of Ref. (21), which is calculated using a collisional density-gradient driven turbulence model. In that case,

$$\Gamma_n^{\text{drift wave}}/n_0 \sim T_e^{1/6} n_0^{2/3} (Rq)^{4/3} \hat{s}^{-3} B_z^{-2} \tag{55}$$

and for Macrotor parameters, $D_n \ll 10^4 \mathrm{cm}^2/\mathrm{sec}$. Thus, the resistivity-gradient-driven turbulence prediction is in better agreement with experimental results from Macrotor,[22]

and offers better prospects for broad applicability, i.e., compare B_z scalings! Finally, since $D_n \sim T^{-5/6} L_\eta^{-4/3} L_s^2 B_z^{-4/3} \sim T^{-5/6} L_\eta^{-4/3} B_z^{2/3} I_p^{-2} \hat{s}^{-2}$ (for q_L not fixed), resistivity-gradient-driven turbulence is a model consistent with particle confinement time τ_p degrading with B_z, but improving with I_p (for q_L not fixed), as observed on the Text tokamak.[6] It also offers the possibility of reconciling high edge temperatures and strong shear with improved particle confinement and steepened temperature gradients.[9]

Although the impurity-gradient-driven turbulence discussed in this paper is primarily electrostatic in character, magnetic fluctuations are also produced. Here, the magnetic fluctuation driven by the tearing parity component of the fluctuation is calculated. Near the resonant surface, parallel electrostatic fields are negligible, since $E_\| \sim -\nabla_\| \hat{\phi}$ and $k_\| \sim x \to 0$. Thus, Ohm's law indicates that

$$\tilde{J}_z \cong -J_{z0}(r) \frac{\tilde{\eta}}{\eta_0} = -J_{z0}(r) \left(\frac{\tilde{\eta}_{\rm sp}}{\eta_{\rm sp,0}} + \frac{\tilde{Z}_{\rm eff}}{Z_{\rm eff,0}} \right), \tag{56}$$

where $J_{z0}(r) = E_0/\eta_0(r)$. The current fluctuation is proportional to the resistivity fluctuation and the local current density. The electromagnetic potential fluctuation is obtained by integrating Eq. (56) using the constant-ψ approximation.[12] Thus

$$\mu_0 \int dx \tilde{J}_z = \Delta' \tilde{\psi}(0), \tag{57}$$

where the domains of integration are restricted by the relevant turbulent mixing lengths. Using Eqs. (44), (47), (30), and (31), it follows directly that

$$\begin{aligned} \left(\frac{\tilde{B}_r}{B_z} \right)_{\rm rms} &\cong \mu_0 \left(\frac{J_{z0}(r)}{2B_z} \right) \left[\frac{\Delta_{\bar{\mathbf{k}}}^{T^2}}{L_\eta} + \frac{\Delta_{\bar{\mathbf{k}}}^{z^2}}{L_z} \right] \\ &= \mu_0 \left(\frac{J_{z0}(r)}{2B_z} \right) \left[\frac{L_s E_0}{L_\eta B_z} (1+\eta_z) \right]^{2/3} \frac{(\chi_T \bar{k}'^2_\|)^{-2/3}}{L_\eta} \left[1 + \eta_z \left(\frac{\chi_T}{\chi_z} \right)^{2/3} \right] \end{aligned} \tag{58}$$

where $\Delta' = -2|k_y|$ for high m fluctuations. Note that the parameter scalings of $(\tilde{B}_r/B_z)_{\rm rms}$ are, using $J_{z0}(r) = E_0/\eta_0(r)$;

$$\begin{aligned} \left(\frac{\tilde{B}_r}{B_z} \right)_{\rm rms} &\sim Z_{\rm eff}^{-1}(r) T^{-1/6} n^{2/3} \left(L_\eta^{-1} + L_z^{-1} \right)^{2/3} L_\eta^{-1} L_s^2 B_z^{-5/3} V_L^{5/3} \\ &\times \left[1 + \eta_z \left(\frac{\chi^T}{\chi^z} \right)^{2/3} \right]. \end{aligned} \tag{59}$$

Thus, $(\tilde{B}_r/B_z)$ is effectively independent of temperature, but is sensitive to $Z_{\rm eff}(r)$, temperature gradient L_T^{-1} and shear, L_s. Also, it is interesting to note that since $\chi_T \gg \chi_z$, relatively modest impurity gradients L_z^{-1} will strongly enhance magnetic fluctuations, and thus the associated magnetic field line stochasticity and anomalous thermal conduction.

The anomalous thermal conduction triggered by magnetic fluctuations associated with resistivity-gradient-driven turbulence can be estimated using the expression, for the case of a collisional plasma, $\chi_\perp \simeq \chi_T \left\langle \tilde{B}_r^2/B_z^2 \right\rangle$. For the $L_z \to \infty$ case, $\chi_\perp \sim J_{z0}(r)^2 \chi_T^{-1/3}$. Hence, for cool, highly resistive edge plasmas, $\chi_\perp$ decreases with increasing radius. This trend is illustrated in Fig. 10, where $\chi_\perp(r)$ is plotted for Macrotor edge parameters and profiles, with $\eta_z = 0$. Note that $\chi_\perp(r) < 10^3 {\rm cm}^2/{\rm sec}$, and that $\chi_\perp(r)$ decreases rapidly with radius. In Fig. 11, the ratio $\chi_\perp(r)/D_n(r)$ is plotted for Macrotor edge parameters and profiles. It is apparent that $\chi_\perp(r)/D_n(r) \sim 10^{-2}$, and decreases with radius. These trends, along with the consequences of the inequality $\tilde{n}/n_0 > \tilde{T}/T_0$ discussed previously, imply that according to this model, *thermal transport in cool, highly resistive edge plasmas is primarily caused by convection.* This result is consistent with recent results from the Caltech[7] and Tosca[8] tokamaks. However, in hotter plasma, where $J_{z0}(r)$, $T_0(r)$ and L_T^{-1} increase, or in the presence of impurity gradients, where $\eta_z \neq 0$, thermal conduction due to magnetic fluctuations may be more significant.

VI. Applications to Tokamak Edge Plasma Phenomena

Previous sections have focused on determining the nonlinear spatial and temporal scales, fluctuation levels, and particle and thermal diffusivities characteristic of saturated resistivity-gradient-driven turbulence. Here, this information is synthesized and used to develop some qualitative insights into tokamak edge plasma phenomena. The specific phenomena considered include:

i) effects of limiter materials on the energy confinement time, τ_E

ii) the density clamp[15] observed during neutral beam co-injection heating.

Limiter materials affect energy confinement in Ohmically heated tokamaks. In the original investigation of impurity-gradient-driven rippling modes, P.H. Rutherford[14] suggested that an impurity profile-dependent particle diffusivity might reconcile the similarity of τ_E scaling in metallic and graphite limiter discharges with their widely disparate radiation losses. The particle diffusivity given in Eq. (56b) depends on the impurity gradient L_z^{-1}, so that a metallic limiter (low sputtering coefficient) will result in improved particle confinement, viz $D_z \sim L_z^{-4/3}$ with L_z relatively large, but thus also in increased high-Z radiation losses. In contrast, a carbon limiter (high sputtering coefficient) will result in increased edge impurity accumulation and increased particle and (convective) energy transport, viz. $D_n \sim L_z^{-4/3}$ with L_z small, but also in reduced high-Z radiation loss. Thus, it appears that the improved confinement associated with the metallic limiter is nullified by the resulting increase in high-Z impurity radiation.

The second phenomenon is the density clamp,[15] which occurs during neutral beam co-injection heating. Originally observed on ISX-B,[15] neutral beam co-injection into discharges with increasing line-averaged density $\bar{n}_e$ (due to gas-puffing) resulted in a saturation of $\bar{n}_e$ shortly after the initiation of injection. This density clamp phenomenon is a consequence of degraded particle confinement. It was also observed that increasing the plasma current I_p resulted in increased saturation values of $\bar{n}_e$. Furthermore, comparison of plasma potential ϕ_p measurements for co-injection and counter-injection discharges from ISX-B indicates that while the plasma potential is negative ($\phi_p < 0$) in counter-injection discharges, it increases and becomes positive ($\phi_p > 0$) near the edge

of co-injection discharges.[23] Therefore, while impurities tend to accumulate on axis in counter-injection discharges, it appears that inward impurity transport is inhibited during co-injection. Thus, a $Z_{\rm eff}(r)$ profile which is peaked at the edge is quite likely.

The resistivity-gradient-driven turbulence particle diffusivity $D_n(r)$, given in Eq. (56b), has properties consistent with several aspects of the density clamp phenomenon. First, $D_n \sim (1+\eta_z)^{4/3}$, so that particle transport is larger in discharges where $Z_{\rm eff}(r)$ is peaked at the edge ($\eta_z > 0$). This is consistent with the increase in D_n during co-injection. Second, $D_n \sim T_i^{-5/6} I_p^{-2}$. Hence, particle confinement is predicted to improve with increased current and edge temperature. These predictions are also consistent with trends observed in experimental studies of particle confinement and the density clamp. Of course, a quantitative test in the context of the density clamp is required to establish the validity of the scenario proposed here. However, such a test requires some knowledge of the impurity profile $Z_{\rm eff}(r)$.

VII. Conclusions

In this paper, the role of impurity dynamics in resistivity gradient driven turbulence and edge plasma phenomena in tokamaks has been investigated. the effects of impurity concentration fluctuations and gradients on the linear evolution and saturation of resistivity gradient driven turbulence have been studied analytically and computationally. Fluctuation levels and particle and thermal diffusivities are calculated and the consequences of these predictions are discussed. The principal results of this paper are:

i) The basic resistivity gradient turbulence model[11] has been extended to include impurity dynamics. Impurity concentration profiles peaked at the edge (on axis) tend to enhance (quench) the turbulence. In most cases, the impurity dynamics dominate the linear evolution of resistivity gradient driven turbulence. It should also be noted that the basic scalings, etc., obtained by Kadomtsev and Pogutse[24] for shearless resistivity gradient driven turbulence differ from those presented here.

ii) The saturated fluctuation levels and thermal and impurity diffusivities have been calculated. The mean-square turbulent velocity is given by

$$\langle \hat{v}_r^2 \rangle = \left[\frac{L_s}{L_\eta} \frac{E_0}{B_z} (1+\eta_z) \right]^2 ;$$

while

$$D^T = \left[\frac{L_s}{L_\eta}\frac{E_0}{B_z}(1+\eta_z)\right]^{4/3} \Big/ \left(\chi_T \bar{k}'^2_{\|}\right)^{1/3}$$

and

$$D^z = \left[\frac{L_s}{L_\eta}\frac{E_0}{B_z}(1+\eta_z)\right]^{4/3} \Big/ \left(\chi_z \bar{k}'^2_{\|}\right)^{1/3}$$

The predictions of the analytic theory are in good agreement with the results of nonlinear, multiple helicity calculations.

iii) The density, temperature, and potential fluctuation levels have been determined. In particular

$$(\tilde{n}/n_0)_{\rm rms} \cong \frac{1}{L_n}\left(\frac{L_s}{L_\eta}\frac{E_0}{B_z}(1+\eta_z)\right)^{1/3}(\chi_z \bar{k}'^2)^{-1/3}$$
$$\approx T^{-5/6} n_0^{1/3} L_n^{-1}\,(1/L_\eta + 1/L_z)\, m_i^{1/6} L_s B_z^{-1/3} V_L^{1/3}$$

$$\tilde{T}/T_0 \cong \frac{1}{L_T}\left(\frac{L_s}{L_\eta}\frac{E_0}{B_z}(1+\eta_z)\right)^{1/3}(\chi_T \bar{k}'^2_{\|})^{-1/3}$$
$$\approx T^{-5/6} n_0^{1/3} L_T^{-1}\,(1/L_\eta + 1/L_z)\, m_e^{1/6} L_s B_z^{-1/3} V_L^{1/3}$$

and

$$\frac{e\hat{\Phi}}{T} = \left(\frac{L_s}{L_\eta}\frac{E_0}{B_z}\right)(1+\eta_z)\Big/(\bar{k}_\theta \rho_s c_s) \approx T^{-1} n_0^0\,(1/L_\eta + 1/L_z)\, L_s V_L.$$

Note $\tilde{n}/n_0 \gg \tilde{T}/T_0$, $\tilde{n}/n_0 \neq e\hat{\Phi}/T_0$, and typically $\tilde{n}/n_0 \gtrsim .2$ while increasing as $r \to a$. These properties are consistent with results from studies of tokamak edge turbulence.[4]

iv) The cross-field particle diffusivity has been calculated, and is given by

$$D_n \cong \left[\frac{E_0}{B_z}\frac{L_s}{L_\eta}(1+\eta_z)\right]^{4/3}\left(\chi_z \bar{k}'^2_{\|}\right)^{-1/3}$$
$$\sim T^{-5/6} n^{1/3} B_z^{-4/3}\frac{q^2R^2}{\hat{s}^2} V_L^{4/3}\,(1/L_\eta + 1/L_z)^{4/3}.$$

Note that typically $D_n \gtrsim 10^4 \mathrm{cm}^2/\mathrm{sec}$ and that $D_n(r)$ increases as $r \to a$. Also, D_n scales favorably with plasma current and unfavorably (for q not held fixed) with B_z. Calculation of magnetic fluctuation levels and the associated thermal diffusivity indicate that the dominant thermal transport mechanism is convection;

i.e., $Q = T\Gamma_n$. These predictions are consistent with results from experiments on the TEXT[6] and Caltech[7] and Tosca[8] tokamaks, respectively.

v) A mechanism which explains the density clamp[15] observed during neutral beam co-injection in terms of an impurity gradient-induced enhancement of the particle diffusivity is proposed. This mechanism requires that $Z_{\text{eff}}(r)$ be peaked at the edge.

In future work, the role of finite diamagnetic frequency effects appropriate to semicollisional parameter regimes, along with the effects of toroidicity and plateau regime collisionality, will be explored. Detailed comparison of experimental results with the theoretical predictions presented in this paper is in progress and will be discussed in a future publication.

Acknowledgments

The authors acknowledge their gratitude to Ch. P. Ritz, D.C. Robinson, W.L. Rowan, C.M. Surko, F. Wagner, A.J. Wootton, S.J. Zweben, and R.C. Isler for numerous stimulating conversations. This research was supported by the U.S. Department of Energy contract #DE-FG05-80ET-53088, and contract #DE-AC05-840R21400 with Oak Ridge National Laboratory.

Appendix: Derivation of Impurity Concentration Evolution Equation

We outline the derivation of $Z_{\rm eff}$ evolution equation (Eq. (4)). The impurity density n_I and hydrogenic ion density n_i each obey a continuity equation of the form,

$$\frac{\partial}{\partial t} n + v_\perp \cdot \nabla n + n \nabla_\parallel v_\parallel = 0. \qquad (A1)$$

Consistent with the electrostatic approximation the nonlinearity retained is due to $\mathbf{E} \times \mathbf{B}$ convection. Due to the presence of a strong ambient magnetic field, and the fact that long wavelength perturbations are considered, the cross field flow $\mathbf{v}_\perp = \dfrac{\mathbf{E} \times \mathbf{B}}{B^2}$ is the same for both hydrogenic and impurity ions. However, the parallel velocity components $v_\parallel$ differ for the two ion species. Using the definition $Z_{\rm eff} = 1 + Z^2 \dfrac{n_I}{n_i}$ and Eq. (A1), we obtain

$$\frac{\partial}{\partial t} Z_{\rm eff} = -\mathbf{v}_\perp \cdot \nabla Z_{\rm eff} - (Z_{\rm eff} - 1) \nabla_\parallel \left(v_{\parallel,I} - v_{\parallel,i} \right), \qquad (A2)$$

where $v_{\parallel,I} - v_{\parallel,i}$ follows from the parallel equations of motion for hydrogenic and impurity ions,

$$n_i m_i \frac{\partial}{\partial t} v_{\parallel,i} = -\nabla_\parallel P_i + n_i e E_\parallel - n_e e \eta_{\rm sp} J_z - n_i m_i \nu_{iI} (v_{\parallel,i} - v_{\parallel,I}), \qquad (A3)$$

$$n_I m_I \frac{\partial}{\partial t} v_{\parallel,I} = -\nabla_\parallel P_I + n_I Z e E_\parallel - n_e e (Z_{\rm eff} - 1) \eta_{\rm sp} J_z + n_i m_i \nu_{iI} (v_{\parallel,i} - v_{\parallel,I}). \qquad (A4)$$

Equation (A4) can be greatly simplified if we note that:

i) The impurity-ion friction terms in each of the two parallel momentum equations (the last terms in Eqs. (A3) and (A4)) are of comparable magnitudes.

ii) Assuming $n_I Z \ll n_i \sim n_e$ and $n_I Z^2 \sim n_i$ (i.e., $Z_{\rm eff} - 1 \sim 1$), the $E_\parallel$ term in Eq. (A4) is smaller than the corresponding term in Eq. (A3),

iii) The impurity inertia is smaller than hydrogenic ion inertia,

iv) The J_z term representing friction with electrons is peaked near the singular surface and negligible in the region where the resistivity perturbations are significant.

The first condition is a consequence of the decoupling of the current perturbations $\tilde{J}_z$ from the resistivity ($\tilde{\eta}$) and potential (ϕ) fluctuations which are centered off the rational

surface for rippling modes and further shifted outward in the nonlinear regime.[11] Items i) through iv) indicate that parallel impurity dynamics is dominated by the balance of the parallel gradient of impurity pressure with the impurity-hydrogenic ion friction. Thus, Eq. (A4) becomes

$$v_{\parallel,i} - v_{\parallel,I} = \frac{T_i \nabla_\parallel \tilde{n}_I}{n_i m_i \nu_{iI}}, \tag{A5}$$

where isothermal ions with $T_i = T_I$ have been assumed. Moreover, since $\gamma \ll k_\parallel v_{Ti}$, constant total pressure is maintained by parallel sound wave propagation, ensuring that $\nabla_\parallel (P_e + P_i + P_I) = 0$. It follows that quasi-neutrality and constant pressure along field lines yield the relation $2\tilde{n}_i + (1+Z)\tilde{n}_I = 0$. Hence, the relative impurity density perturbation is significantly larger than the relative hydrogenic ion density perturbation, and $\tilde{Z}_{\text{eff}} \cong Z^2 \frac{\tilde{n}_I}{n_i}$. Using this relation and $\nu_{iI} = (Z_{\text{eff}} - 1)\nu_{ii}$, we obtain Eq. (4) from Eqs. (A2) and (A5).

References

1. C.M. Surko and R.E. Slusher, Science 221, 817 (1983).
2. S.J. Zweben and R.W. Gould, Nucl. Fusion **23**, 1625 (1983).
3. S.J. Levinson, J.M. Beall, E.J. Powers, and R.D. Bengtson, Nucl. Fusion **24**, 527 (1984).
4. Ch.P. Ritz, Roger D. Bengtson, S.J. Levinson, and E.J. Powers, Phys. Fluids **27**, 2956 (1984).
5. A.J. Wootton, H. Howe, P.H. Edmonds, C.H. Ma, P.K. Mioduszewki, K. Yokoyama, submitted to Nucl. Fusion (1985).
6. William L. Rowan, C.C. Klepper, Ch.P. Ritz, Roger D. Bengtson, K.W. Gentle, P.E. Phillips, T.L. Rhodes, B. Richards, and A.J. Wootton, submitted to Nucl. Fusion (1985).
7. P.C. Liewer, J.M. McChesney, S.J. Zweben, and R.W. Gould, Phys. Fluids **29**, 309 (1986).
8. A. Howling, A. Coté, E.J. Doyle, D.E. Evans, and D.C. Robinson, *Proceedings of the 12th European Conference on Controlled Fusion and Plasma Physics*, Budapest, Hungary, 1985, edited by L. Póas and A. Montvai (European Physical Society, Budapest, 1985), Vol. I, p. 311.
9. F. Wagner, G. Fussmann, T. Grave, M. Keilhacker, M. Kornherr, K. Lackner, K. McCormick, E.R. Miller, A. Stäbler, G. Becker, K. Bernhardi, U. Ditte, A. Eberhagen, O. Gehre, J. Gernhard, G.v. Gierke, E. Glock, O. Gruber, G. Haas, M. Hesse, G. Janeschitz, F. Karger, S. Kissel, O. Klüber, G. Lisitano, H.M. Mayer, D. Meisel, V. Mertens, H. Murmann, W. Poschenrieder, H. Rapp, H. Röhr, F. Ryter, F. Schneider, G. Siller, P. Smeulders, F. Sóldner, E. Speth, K.H. Steuer, Z. Szymanski, and O. Vollmer, Phys. Rev. Lett. **53**, 1453 (1984).
10. J.D. Callen, B.A. Carreras, P.H. Diamond, M.E. Benchikh-Lehocine, L. Garcia, and H.R. Hicks, in Plasma Physics and Controlled Nuclear Fusion Research, 1982. (IAEA, Vienna, 1983), Vol. 1, p. 297.
11. L. Garcia, P.H. Diamond, B.A. Carreras, and J.D. Callen, Phys. Fluids **28**, 2147 (1985).

12. H.P. Furth, J. Killeen and M.N. Rosenbluth, Phys. Fluids **6**, 459 (1963).

13. B.A. Carreras, P.W. Gaffney, H.R. Hicks, and J.D. Callen, Phys. Fluids **26**, 1231 (1982).

14. P.H. Rutherford, in *Physics of Plasma Close to Thermonuclear Conditions*, ed. by B. Coppi, et al., (Pergamon Press, New York, 1981), Vol. I, p. 143.

15. M. Murakami, D.W. Swain, S.C. Bates, C.E. Bush, L.A. Charlton, J.L. Dunlap, G.R. Dyer, P.H. Edmonds, A.C. England, H.H. Haselton, J.T. Hogan, H.C. Howe, D.P. Hutchinson, R.C. Isler, T.C. Jernigan, S. Kasai, H.E. Ketterer, J. Kim, P.W. King, E.A. Lazarus, J.F. Lyon, C.H. Ma, J.T. Mihalczo, J.K. Munro, A.P. Navarro, G.H. Neilson, D.R. Overbey, V.K. Paré, M.J. Saltmarsh, S.D. Scott, J. Sheffield, J.E. Simpkins, W.L. Stirling, C.C. Tsai, R.M. Wieland, J.B. Wilgen, W.R. Wing, R.E. Worsham, B. Zurro, in *Plasma Physics and Controlled Nuclear Fusion Research*, 1980 (IAEA, Vienna, 1981), Vol. I, p. 377.

16. H.R. Strauss, Phys. Fluids **19**, 134 (1976).

17. T.S. Hahm, P.W. Terry and P.H. Diamond, Proceedings of Annual Controlled Fusion Theory Conference (University of Wisconsin, Madison, 1985), p. 2R-15.

18. J.W. Connor, Nucl. Fusion **26**, 517 (1986).

19. P.W. Terry, P.H. Diamond, K.C. Shaing, L. Garcia, and B.A. Carreras, Phys. Fluids **29**, 2501 (1986).

20. L. Garcia, H.R. Hicks, B.A. Carreras, L.A. Charlton, and J.A. Holmes, submitted to J. Comput. Phys. (1985).

21. P.W. Terry and P.H. Diamond, Phys. Fluids **28**, 1419 (1985).

22. S.J. Zweben, C.R. Menyuk, and R.J. Taylor, Phys. Rev. Lett. **42**, 1270 (1979); S.J. Zweben and R.J. Taylor, Nucl. Fusion **21**, 193 (1981).

23. M. Murakami, P.H. Edmonds, G.A. Hallock, R.C. Isler, E.A. Lazarus, G.H. Neilson, A.J. Wootton, J.D. Bell, C.E. Bush, A Carnevali, B.A. Carreras, J.L. Dunlap, A.C. England, W.L. Gardner, R.L. Hickok, H.C. Howe, D.P. Hutchinson, W.C. Jennings, R.R. Kindsfather, R.A. Langley, C.H. Ma, J. Mathew, P.K. Mioduszewski, J.K. Munro, V.K. Paré, M.J. Saltmarsh, S.D. Scott, D.J. Sigmar, M.L. Simpson, C.E. Thomas, R.M. Wieland, W.R. Wing, K.E. Yokoyama in *Plasma*

Physics and Controlled Nuclear Fusion Research, 1984 (IAEA, Vienna, 1985) Vol. I, p. 87.

24. B.B. Kadomtsev and O.P. Pogutse; *Reviews of Plasma Physics* Vol. V (Consultants Bureau, New York 1970).

TABLE I

Macrotor parameters:

Various predicted fluctuation levels and particle diffusivity at saturation for typical Macrotor parameters (three different Z_{eff} profiles considered).

$L_\eta = 0.3a$, $L_s = 4.2a$, $r_s = 0.77a$, $S(0) = 10^5$

$\bar{\chi}_\parallel = \chi_T \tau_R / R_0^2 = 2.5 \times 10^5$, $R_0 = 90\text{cm}$, $a = 45\text{cm}$, $n(0) = 10^{13}\text{cm}^{-3}$

$B_T = 2kG$, $T_e(r_s) = 15\text{eV}$, $\eta(r_s) = 6.3\eta(0)$,

$C_s = 4.9 \times 10^6 \text{cm/sec}$, $\Omega_i = 1.9 \times 10^7/\text{sec}$, $\rho_s = 0.26\text{cm}$

L_z/a	$r_{5/2}/a$	L_η/a	$\bar{E}\tau_R^2/a^2$	$\left(\frac{\tilde{\eta}}{\eta_0}\right)_{\text{rms}}$	$\left(\frac{\tilde{T}}{T_0}\right)_{\text{rms}}$	$\left(\frac{e\tilde{\Phi}}{T_e}\right)_{\text{rms}}$	$D_n = D_z$
0.40	0.74	1.30	610	8.5×10^{-2}	5.7×10^{-2}	6.9×10^{-2}	5.5×10^4
∞	0.77	1.62	268	5.1×10^{-2}	3.4×10^{-2}	4.6×10^{-2}	3.6×10^4
-0.65	0.79	1.89	87	2.2×10^{-2}	1.5×10^{-2}	2.6×10^{-2}	1.9×10^4

Figure Captions

Fig. 1 Linear growth rates from the initial value code as a function of L_z (Z_{eff}-gradient scale length).

Fig. 2 Comparison between the initial value code results and the shooting code results.

Fig. 3 The structures of the eigenfunction (ϕ) and the effective potential of Eq. (17).

Fig. 4 Various eigenmode $\left(\phi, \tilde{T}_e, \tilde{Z}_{\text{eff}}\right)$ structures for the most unstable modes.

Fig. 5 The equilibrium profiles of T_e, Z_{eff}, η, and q for three different values of L_z.

Fig. 6 Mean-square radial velocity as a function of radius for three different values of L_z.

Fig. 7 Various relative fluctuation levels $\left(\tilde{n}/n_0, e\tilde{\Phi}/T_0, \tilde{T}/T_0\right)$ at saturation as functions of minor radius for $L_z = \infty$.

Fig. 8 Various relative fluctuation levels $\left(\tilde{n}/n_0, e\tilde{\Phi}/T_0, \tilde{T}/T_0\right)$ at saturation as functions of radius for $L_z = L_\eta$.

Fig. 9 Particle diffusivity at saturation as a function of radius.

Fig. 10 Thermal conductivity at saturation as a function of radius.

Fig. 11 The ratio of thermal conductivity to particle diffusivity as a function of radius.

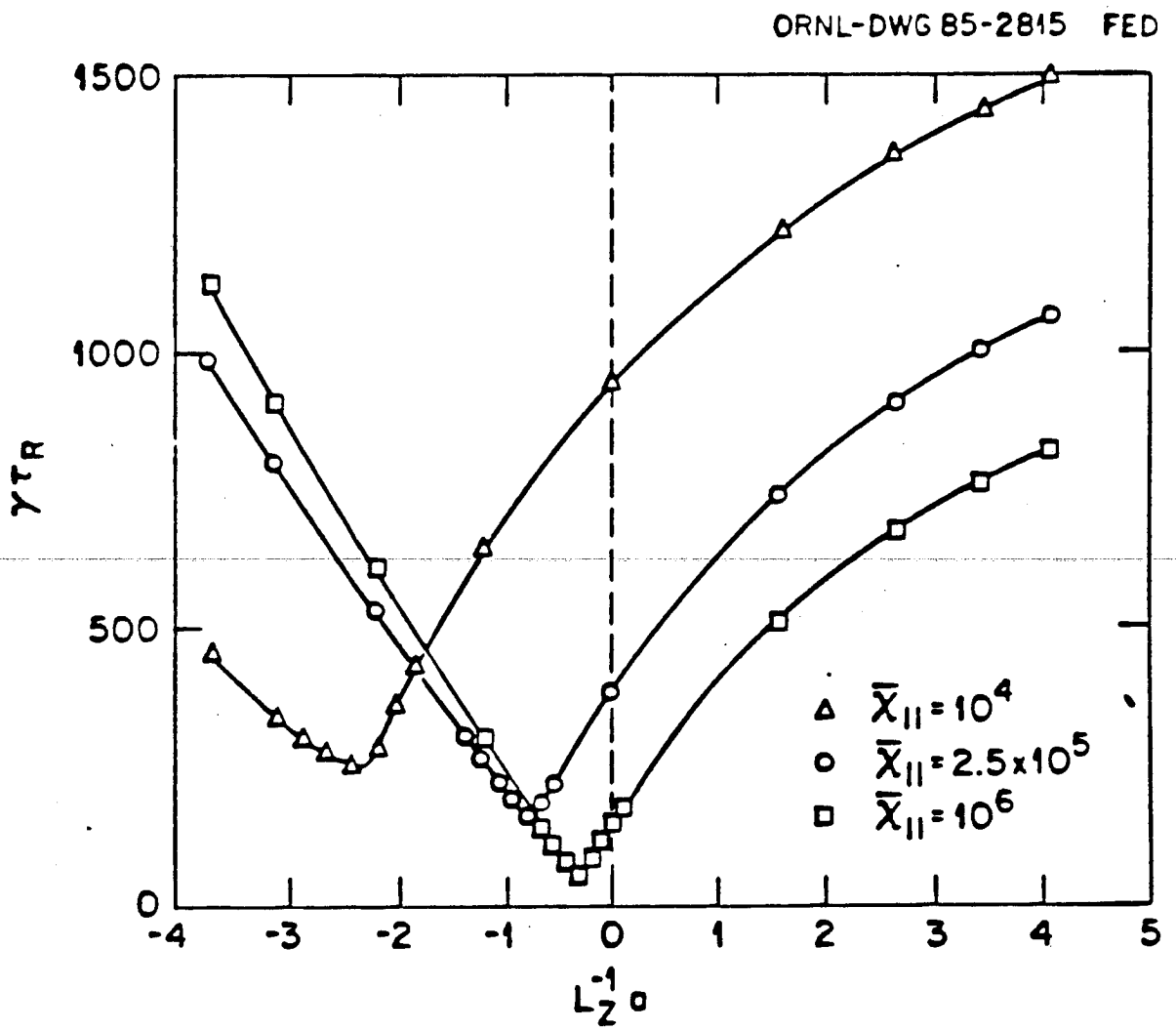
ORNL-DWG 85-2815 FED
1500
1000
500
0
$\gamma\tau_R$
-4
-3
-2
-1
0
1
2
3
4
5
$L_z^{-1}a$
$\bar{\chi}_{11} = 10^4$
$\bar{\chi}_{11} = 2.5 \times 10^5$
$\bar{\chi}_{11} = 10^6$

Fig. 1

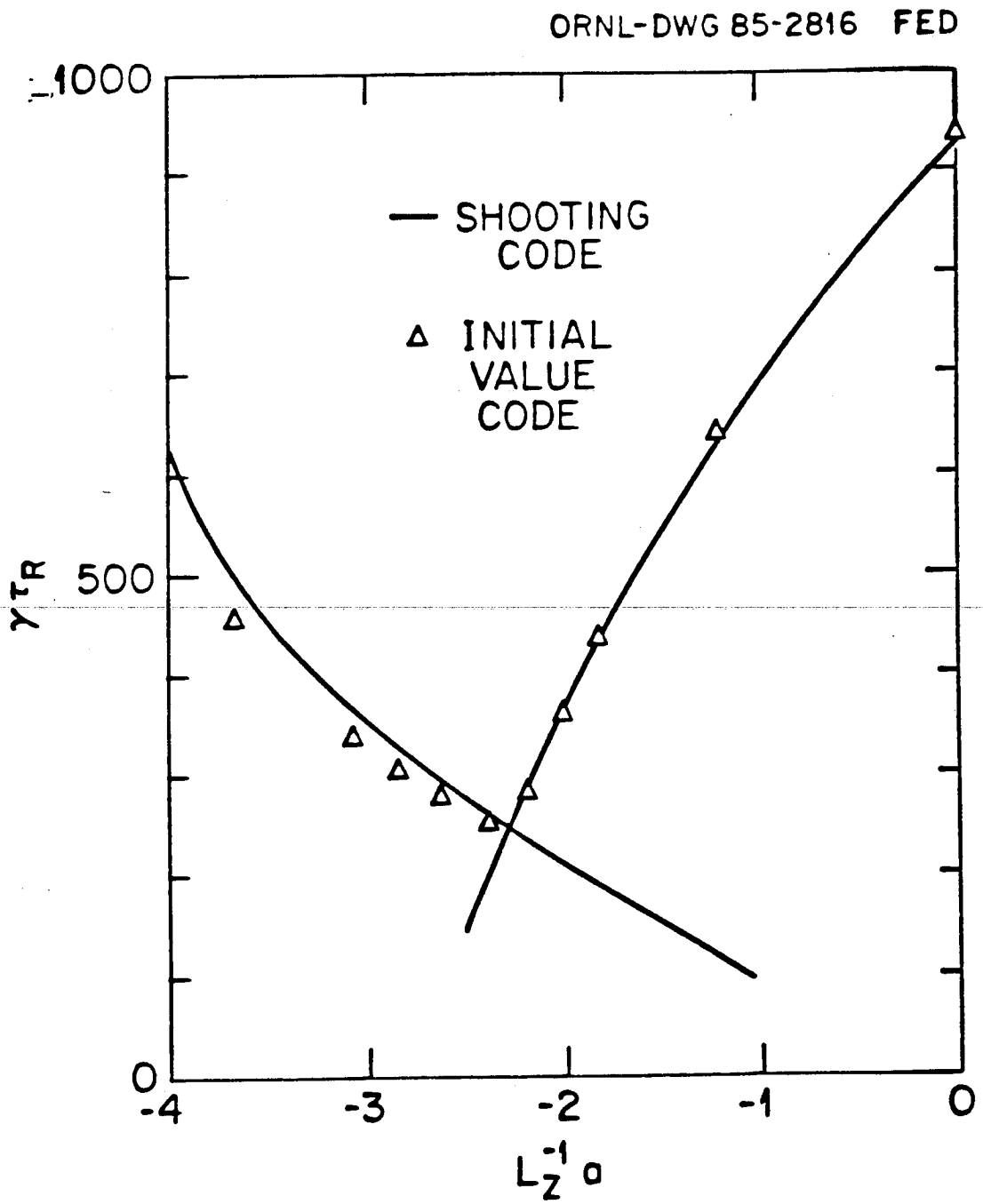
ORNL-DWG 85-2816 FED
1000
500
0
$\gamma\tau_R$
— SHOOTING CODE
△ INITIAL VALUE CODE
-4
-3
-2
-1
0
$L_z^{-1}a$

Fig. 2

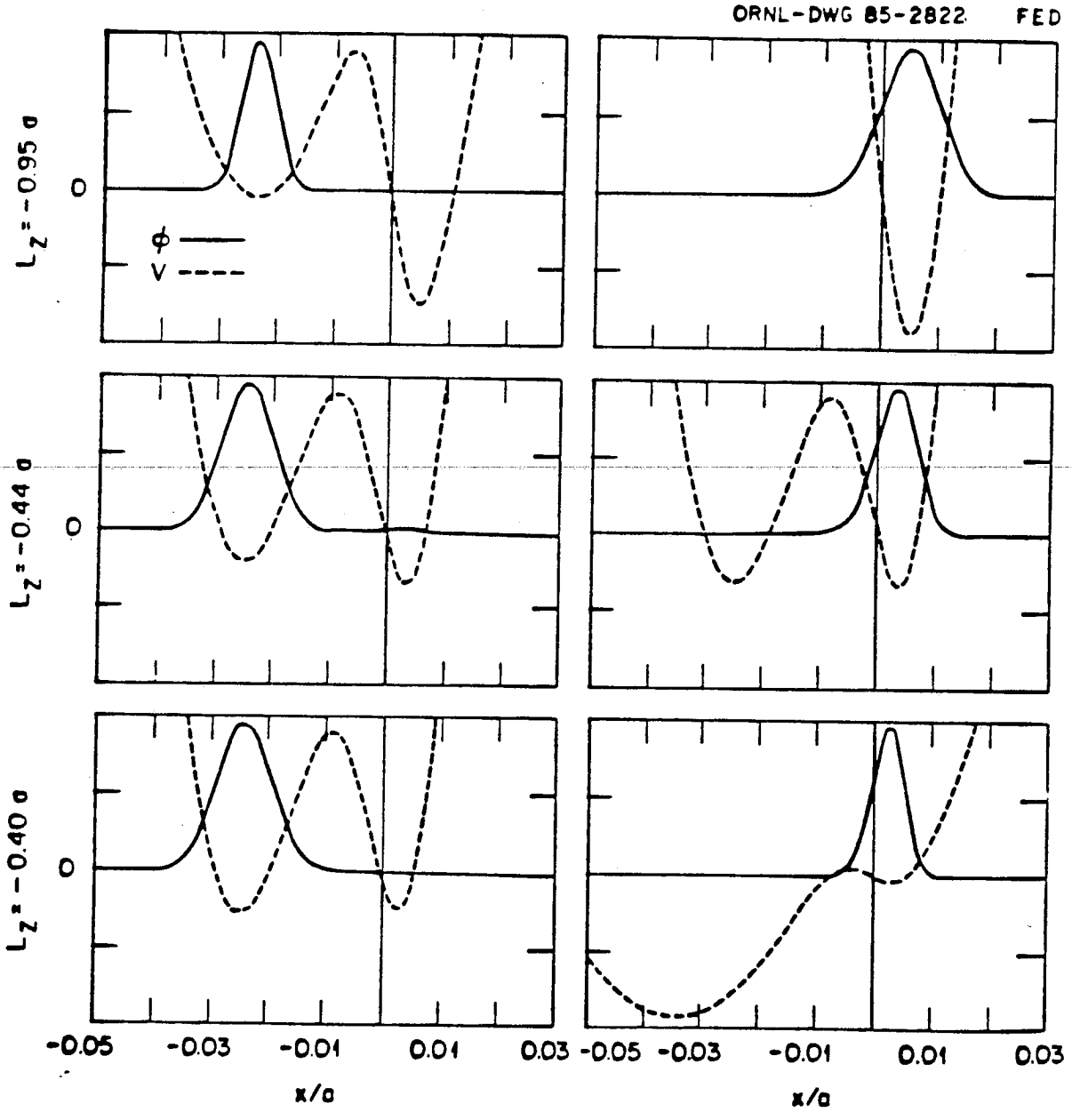
ORNL-DWG 85-2822 FED
L_z=-0.95 a
L_z=-0.44 a
L_z=-0.40 a
0
φ
V
-0.05
-0.03
-0.01
0.01
0.03
x/a

Fig. 3

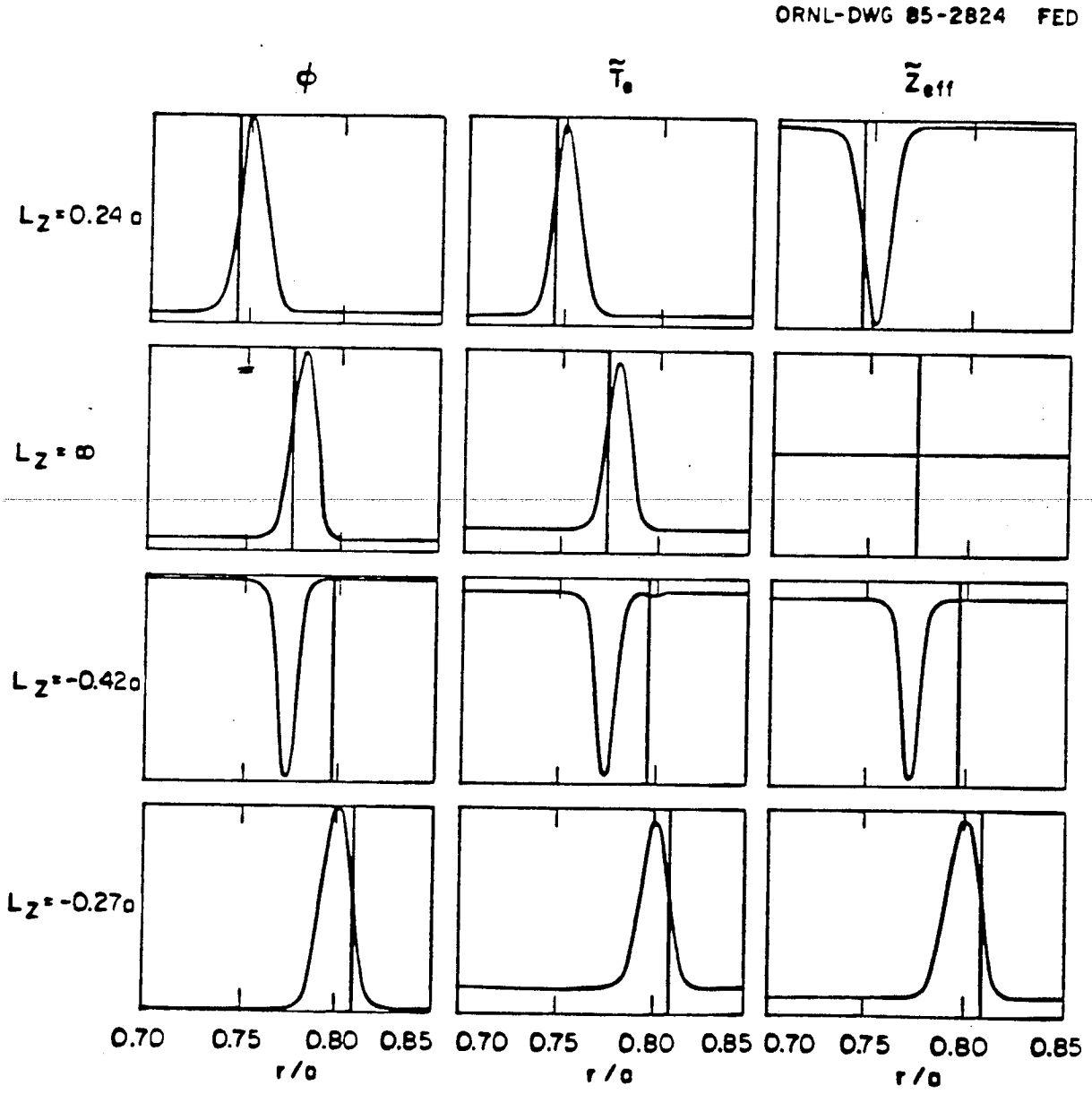
ORNL-DWG 85-2824 FED
ϕ
$\tilde{T}_e$
$\tilde{Z}_{eff}$
$L_z = 0.24\,a$
$L_z = \infty$
$L_z = -0.42a$
$L_z = -0.27a$
0.70 0.75 0.80 0.85
r/a

Fig. 4

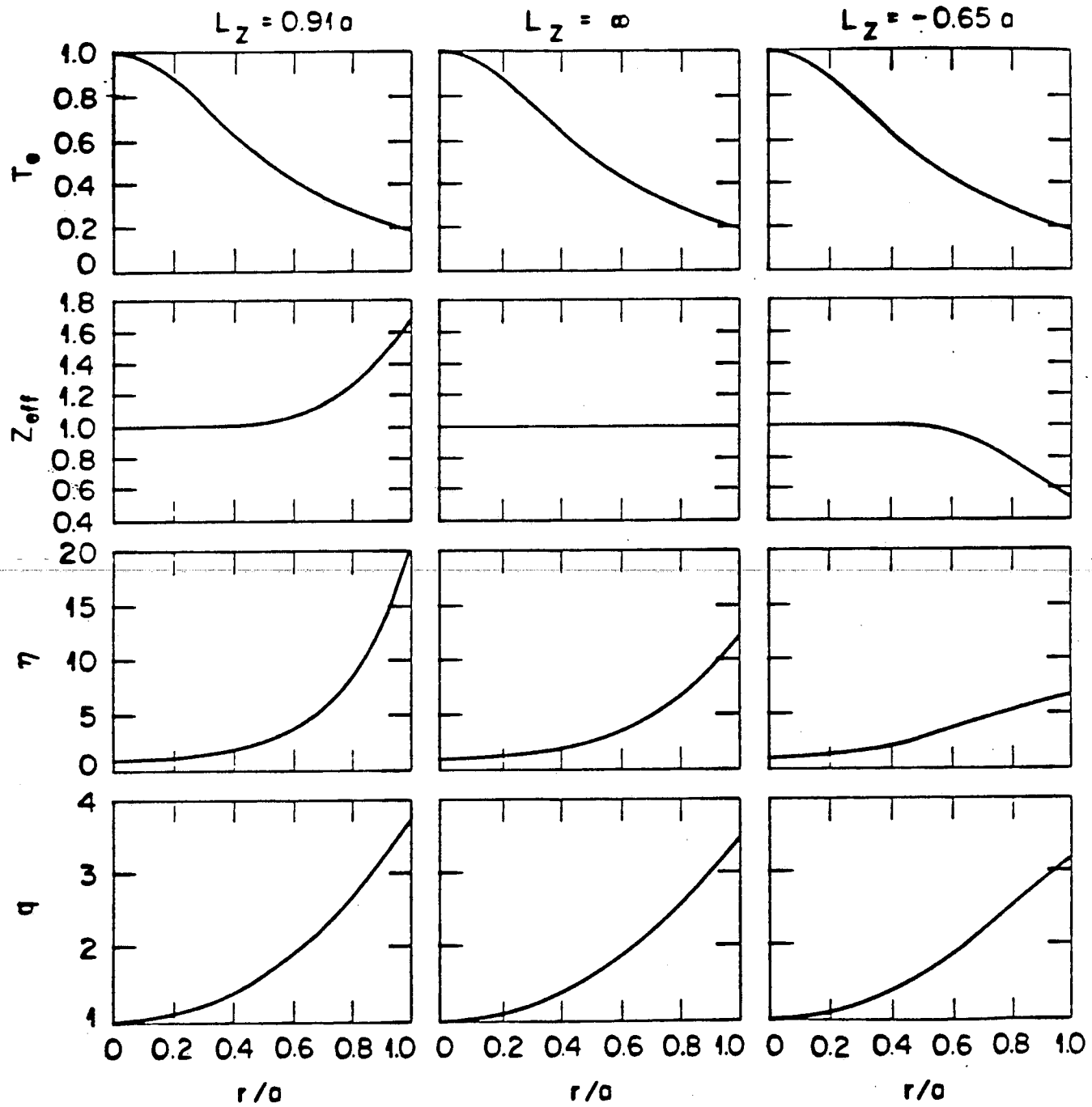

Fig. 5

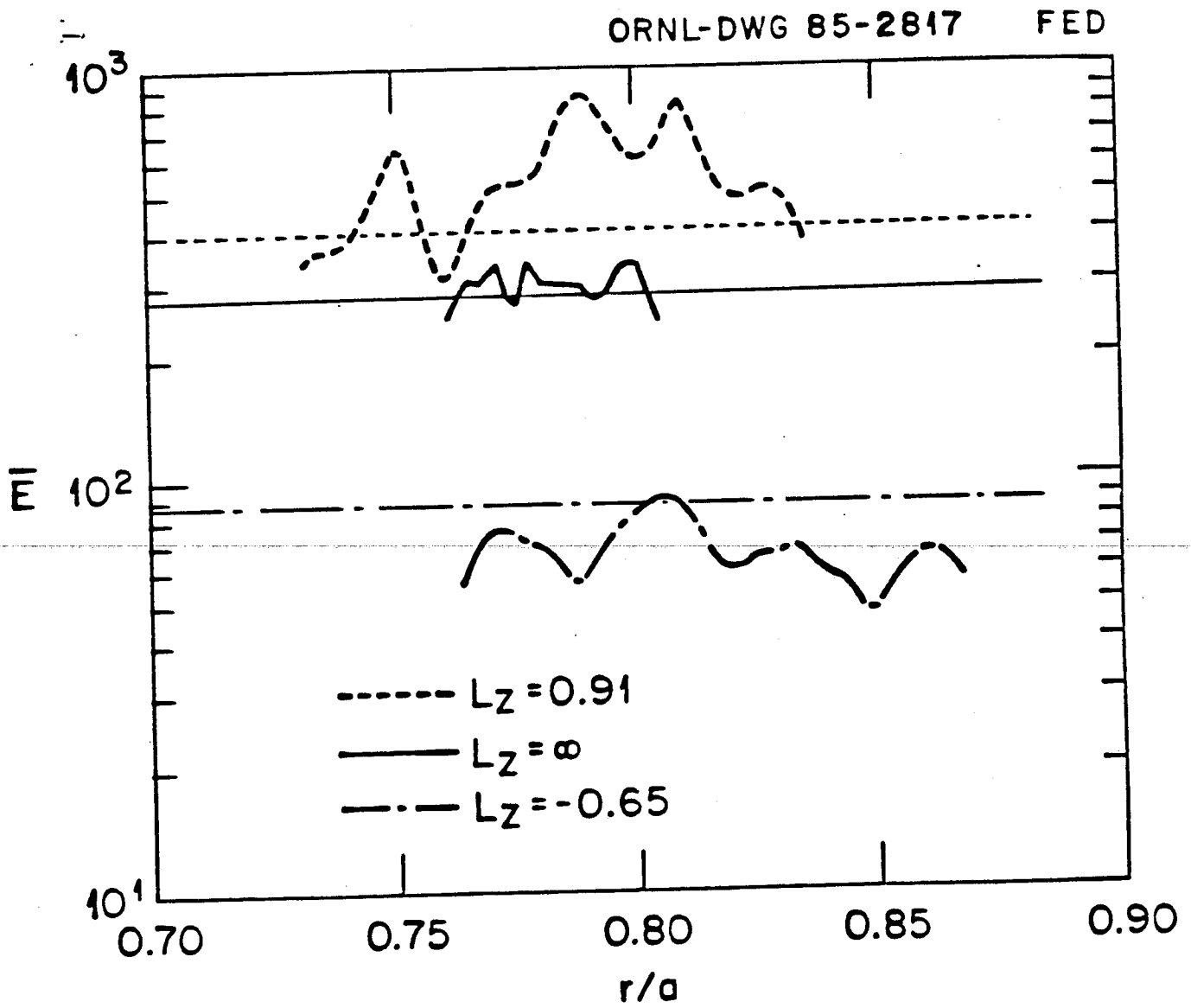
ORNL-DWG 85-2817 FED
10^3
$\bar{E}$ 10^2
10^1
$L_Z = 0.91$
$L_Z = \infty$
$L_Z = -0.65$
0.70
0.75
0.80
0.85
0.90
r/a

Fig. 6

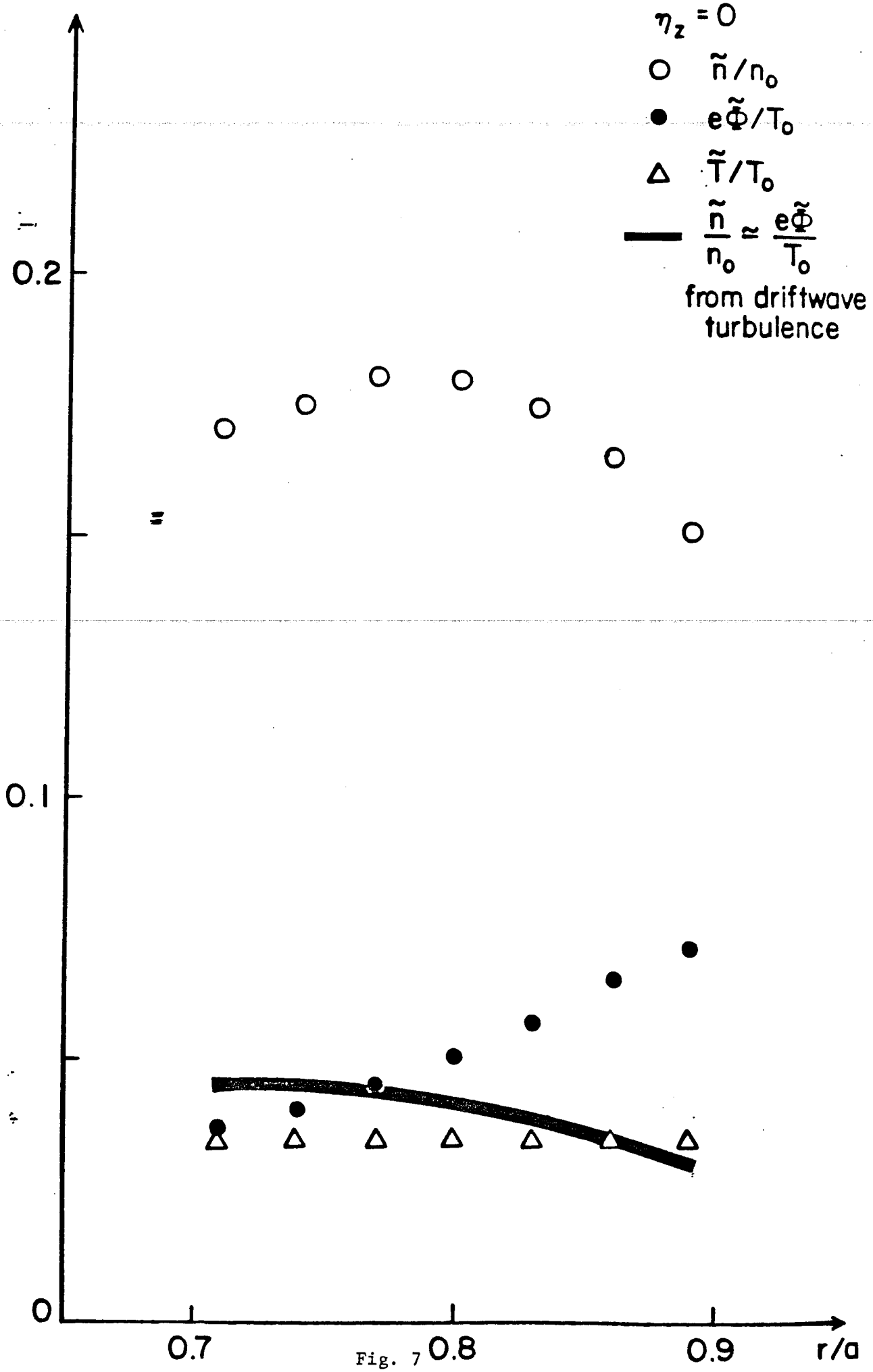
$\eta_z = 0$
$\tilde{n}/n_o$
$e\tilde{\Phi}/T_o$
$\tilde{T}/T_o$
$\frac{\tilde{n}}{n_o} \simeq \frac{e\tilde{\Phi}}{T_o}$
from driftwave turbulence
0.2
0.1
0
0.7
0.8
0.9
r/a

Fig. 7

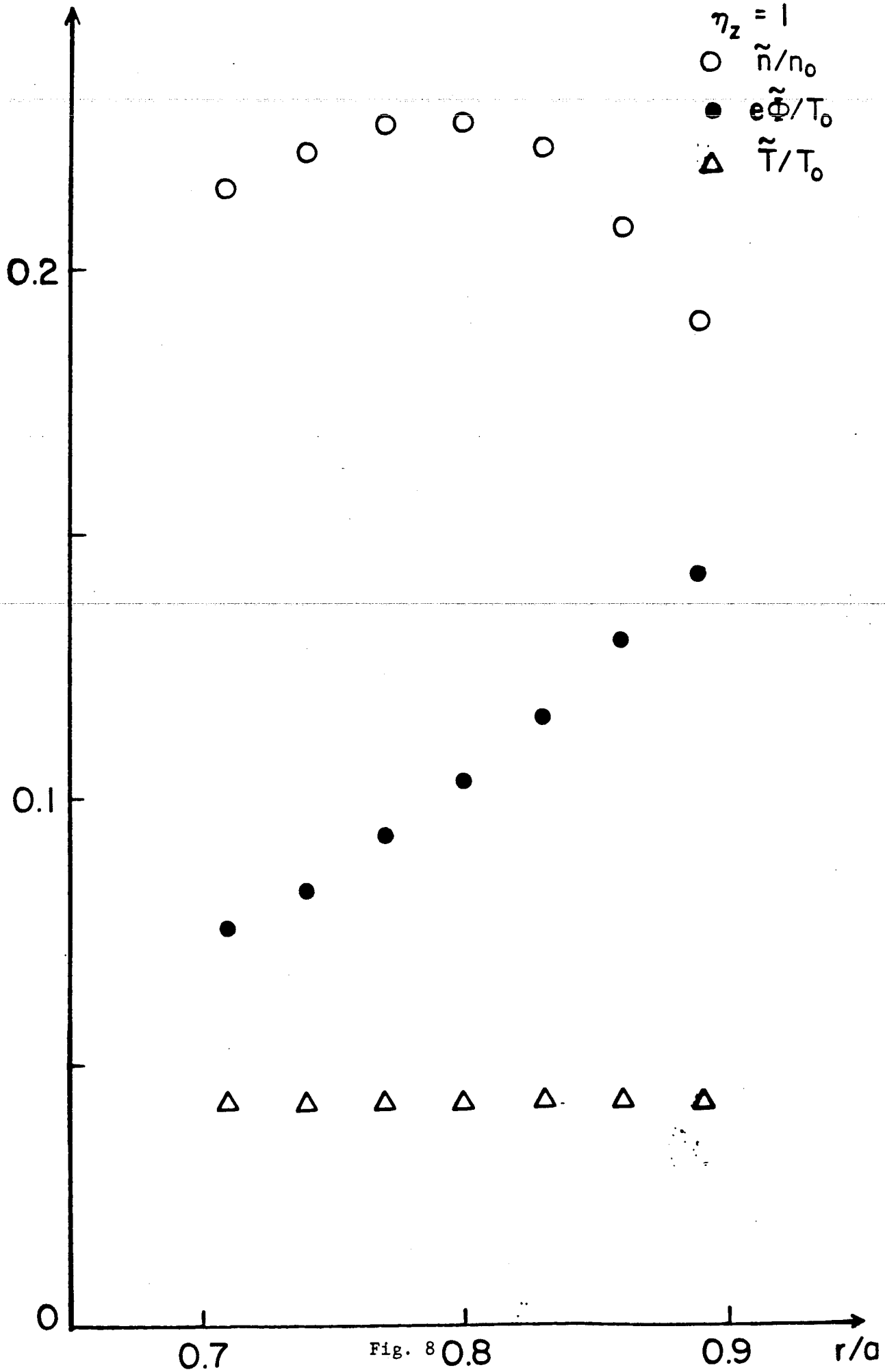

Fig. 8

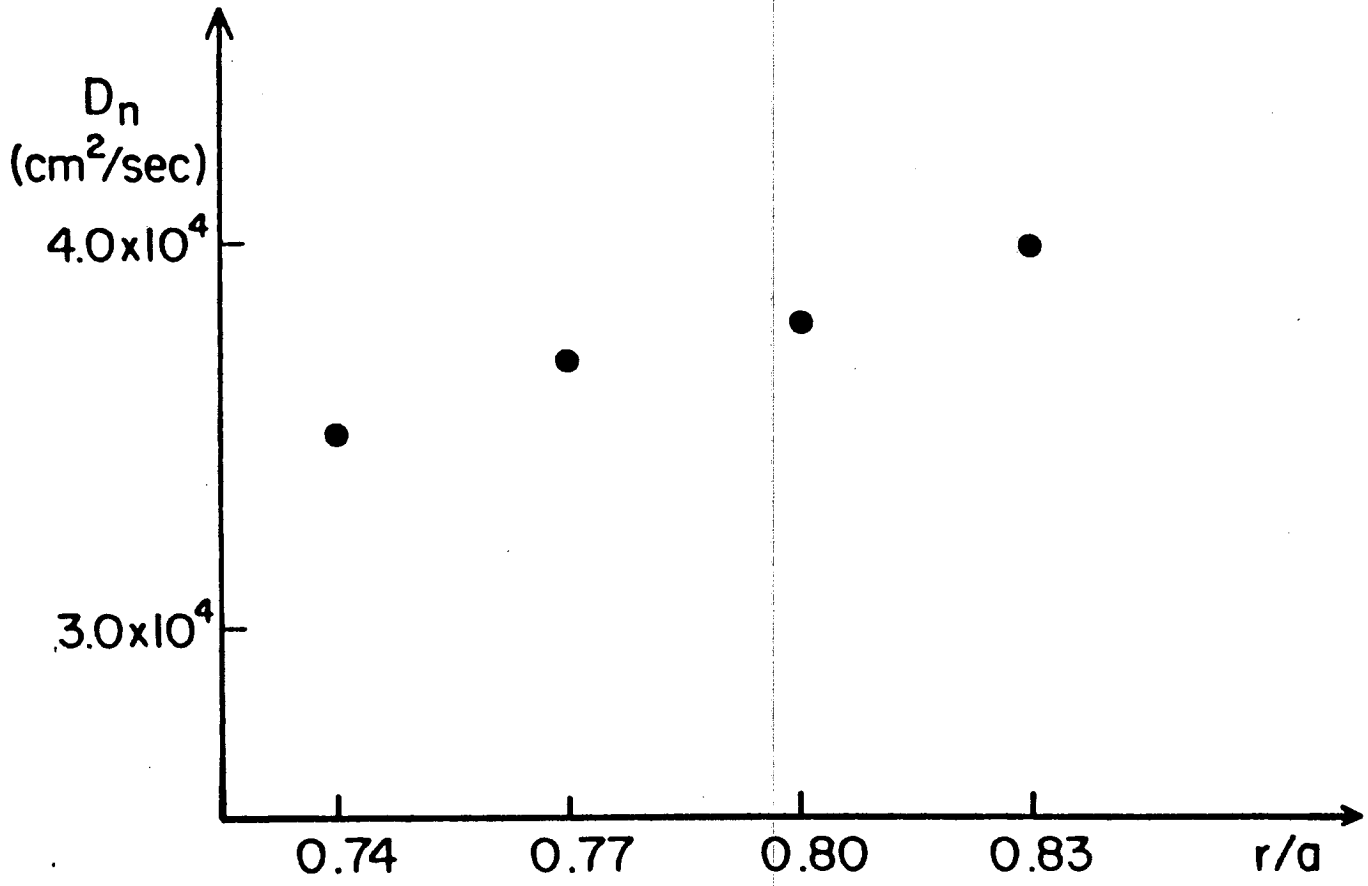

Fig. 9

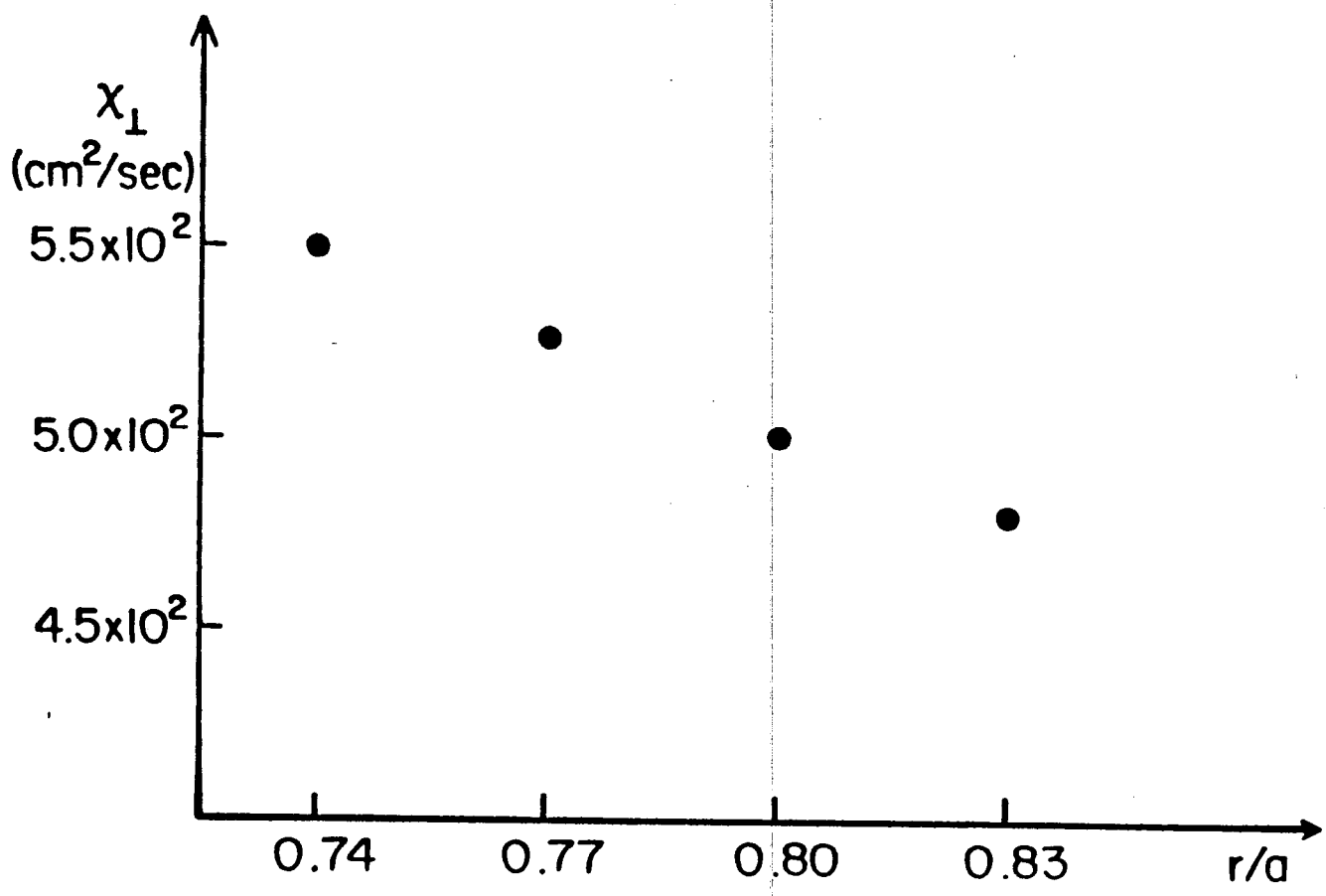

Fig. 10

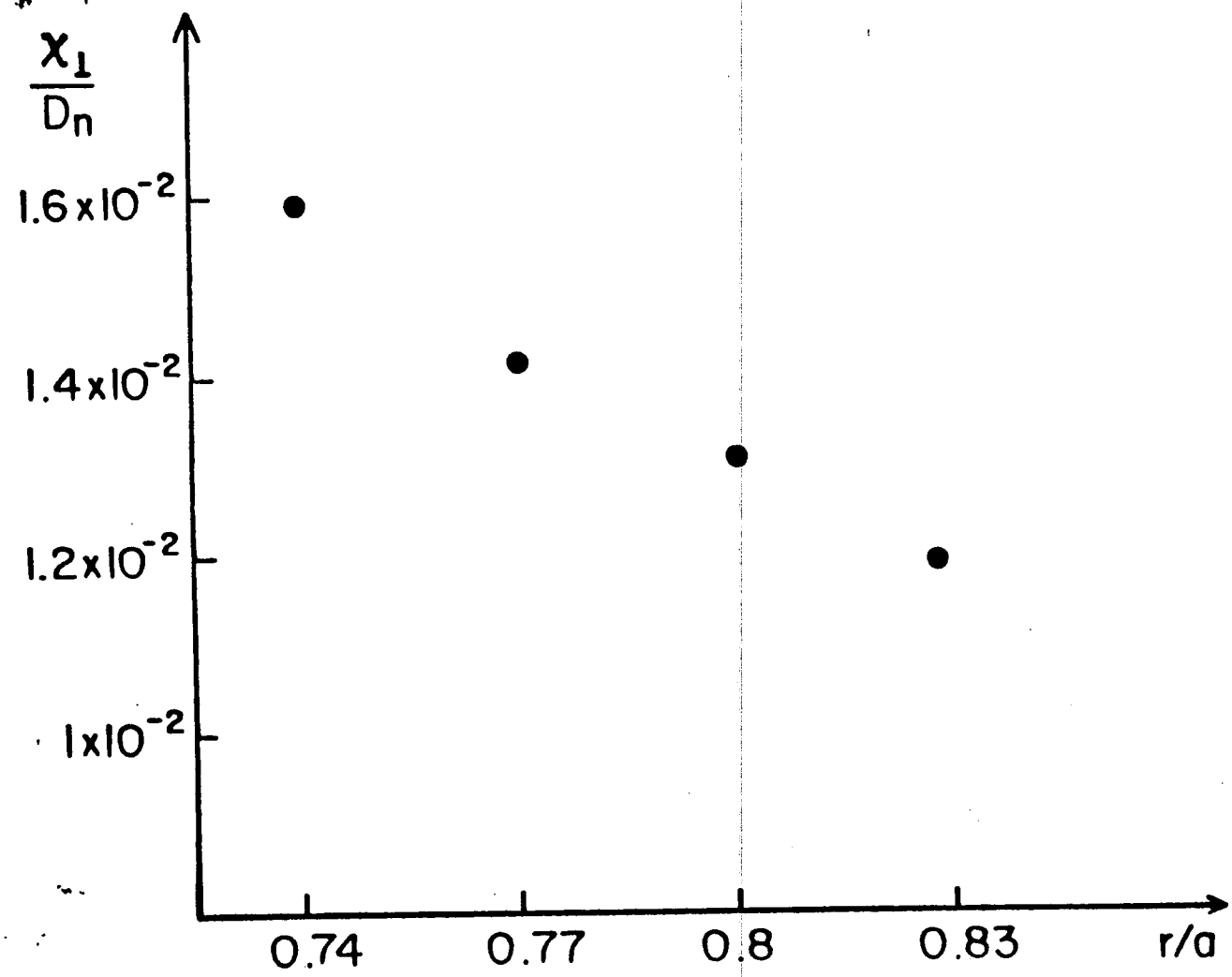

Fig. 11